The role of crustal anatexis in porphyry copper ore formation during flat-slab subduction: Insights from the Laramide Belt, SW USA

Thomas N Lamont[1], Matthew A Loader[2], Nick M W Roberts[3], Frances J Cooper[1,4], Jamie J Wilkinson[2,5], Dan Bevan[1,6], Adam Gorecki[7], Anthony Kemp[6], Tim Elliott[1], Nicholas J Gardiner[8] and Simon Tapster[3]

[1]School of Earth Sciences, Wills Memorial Building, University of Bristol, Bristol, UK

[2]London Centre for Ore Deposits and Exploration (LODE), Natural History Museum, London, UK

[3]Geochronology and Tracers Facility, British Geological Survey, Nottingham, UK

[4]Department of Earth Sciences, University College London, UK

[5]Department of Earth Science and Engineering, Imperial College London, UK

[6]Centre for Exploration Targeting, School of Earth Sciences, University of Western Australia, Perth, Australia

[7]BHP, Tucson, Arizona, USA

[8]School of Earth and Environmental Sciences, University of St Andrews, St Andrews, UK

Key Points:

1. The Laramide porphyry province in Arizona formed during a period of flat-slab subduction of the Farallon plate beneath North America between ca. 80–50 Ma.
2. Laramide granitic rocks in Arizona have isotopic signatures and zircon inheritance suggesting they are derived from Proterozoic aged crust.
3. Proterozoic crustal rocks were pre-enriched in copper and underwent water-fluxed anatexis between 73–60 Ma coincident with flat-slab subduction ca. 75–65 Ma and porphyry genesis ca. 73–56 Ma.

THIS MANUSCRIPT HAS NOT BEEN PEER REVIEWED YET. IT IS SUBMITTED TO 'NATURE GEOSCIENCE'.

ABSTRACT

The prevailing paradigm for the formation of porphyry copper deposits along convergent plate boundaries involves deep-crustal differentiation of metal-bearing juvenile magmas derived from the mantle-wedge above a subduction zone. However, many major porphyry districts formed during periods of flat-slab subduction when the mantle-wedge would have been reduced or absent, leaving unclear the source region of the ore-forming magmas. To resolve this paradox, we investigate deep crustal processes during the genesis of the Laramide Porphyry Province of Arizona, which formed between 80–50 Ma during flat-slab subduction of the Farallon Plate beneath North America. We show that: (1) Laramide granitic rocks have isotopic signatures implying a crustal origin suggesting that they were derived from Proterozoic aged crust; and (2) Proterozoic crustal rocks were pre-enriched in copper and underwent water fluxed anatexis between 73–60 Ma at a geothermal gradient of ~28°C/km, coincident with the zenith of granitic magmatism, porphyry genesis (73–56 Ma) and flat-slab subduction (75–65 Ma). To explain the formation of the Laramide Porphyry Province, we propose that volatiles derived from the leading edge of the Farallon flat-slab promoted anatexis of mafic (garnet pyroxenite and amphibolite) and felsic pre-enriched lower crust, without necessarily requiring significant juvenile mantle-wedge derived magmatism.

INTRODUCTION

There remains profound uncertainty concerning the deep-crustal processes responsible for the formation of porphyry copper deposits (PCDs) along convergent plate boundaries. In these settings, the development of volatile-rich magmas that typify PCDs are classically explained by extensive lower-crustal differentiation of juvenile basaltic melts derived from metasomatism of the mantle wedge above a dehydrating subducting slab[1,2] (Fig. 1a). Magma fractionation depth proxies (high Sr/Y, La/Yb and (Eu/Eu*)/Yb) suggest that porphyry copper-ore formation is favoured in thickened continental crust within mature compressional arcs[3,4,5]. Such deeply differentiated magmas are interpreted to contain high concentrations of volatiles (H_2O, CO_2, Cl and S) which are critical in controlling the ultimate enrichment of copper and other metals in PCDs formed in the shallow crust[1,2].

However, many major porphyry districts (e.g., Resolution, Arizona, USA; Río Blanco-Los Bronces and La Escondida, Chile) formed during periods of flat-slab subduction[4,6,7] when the subducting plate was underthrust at a shallow angle or even horizontally beneath the overriding plate. This geodynamic scenario occurs when either: (1) young, warm and buoyant oceanic lithosphere is subducted; or (2) the rate of trench retreat is greater than the rate of slab-rollback in a fixed mantle reference frame[8]. During such periods, the mantle wedge (the assumed ultimate PCD magma source in traditional models) would have been significantly reduced or absent, leaving it unclear from where the ore-forming magmas were derived (Fig. 1b). To address this paradox, we investigate the Late Cretaceous-Palaeocene Laramide Orogeny in Arizona, southwest USA (Fig. 2a-b), which hosts the world's second largest porphyry

copper province[7,9] and formed during a period of flat-slab subduction. We show that water fluxed anatexis of Proterozoic crustal rocks that were heterogeneously pre-enriched in copper is fundamental to the genesis of Laramide granites and their associated PCDs.

Flat-Slab Subduction and Crustal Anatexis During the Laramide Orogeny

The Laramide Orogeny defines a period of crustal thickening and magmatism that occurred during flat-slab subduction of the Farallon Plate beneath western North America between ca. 90 and 40 Ma (Fig. 1b). Flat-slab subduction was likely due to intersection of the Shatsky-Hesk oceanic plateau with the trench at ca. 90 Ma[10], in combination with westward movement of North America with respect to a fixed mantle reference frame[8]. In Arizona, the Laramide Orogen is characterized by: (1) contemporaneous hornblende-bearing ('I-type') and garnet-muscovite-bearing ('S-type') granitic intrusions spanning ca. 78–50 Ma[11,12]; (2) PCDs that formed between ca. 73–53 Ma[7,8,13] (Table S1); and (3) contractional structures active between ca. 80–60 Ma[14,15,16]. All these features are concentrated in a series of NW–SE trending belts (the Colorado Plateau Transition Zone, CPTZ; Fig. 2b) along the western margin of the relatively undeformed Colorado Plateau[9,13].

Along the CPTZ, most PCDs (e.g., Ray, Resolution, Morenci; Fig. 2b) are associated with I-type intrusions, which often display elevated whole-rock Sr/Y, La/Yb and (Eu/Eu*)/Yb ratios[5] typical of deeply-fractionated "fertile" PCD-related magmas (Table S2). These I-type magmas are traditionally explained by mantle wedge-derived melts strongly interacting with the crust[17,18,19]. However, Laramide volcanism along the CPTZ terminated ~2–5 million years prior to PCD formation, suggesting the ore-forming intrusions developed during a distinct phase of plutonism in a volcanically inactive arc segment. Interestingly, several deposits (e.g., Diamond Joe, Texas Canyon; Fig 2b), are associated with peraluminous S-type granitic intrusions, which display comparable fertility indices to the I-type granites (Fig. 2c-d; Table S2). Because similarly peraluminous Laramide intrusions are clearly derived from crustal sources[20,21,22,23], it implies that crustal anatexis may be important for regional metallogeny.

Further insights into the geodynamic setting and sources of Laramide granitic magmas can be gleaned from whole-rock Sr–Nd–Pb data[17,18,19] and Hf-in-zircon isotopes[20,21,24] (Fig. 3). A compilation of igneous rocks younger than 140 Ma from the southwest USA and northwest Mexico (Fig. 3a; Table S3) shows: (1) decreasing $\varepsilon Nd_{(t)}$ between 110–80 Ma reflecting a progressively diminishing contribution of mantle-wedge derived magma; (2) negative (i.e. unradiogenic) $\varepsilon Nd_{(t)}$ during the Laramide Orogeny (ca. 80–40 Ma) which overlaps with the range of Proterozoic basement values, consistent with a significant component being derived from such crustal sources; and (3) increasing $\varepsilon Nd_{(t)}$ after ca. 40 Ma, suggesting an increasing contribution of juvenile magma

associated with renewed asthenospheric mantle melting following Farallon slab rollback or foundering.

In Arizona, both I-type and S-type Laramide intrusions (ca. 78–50 Ma) fit this isotopic framework, characterized by unradiogenic Nd signatures (I-type εNd(t) = -0.2 to -13.5; S-type εNd(t) = -3.0 to -18.4; Fig. 3b-d) and >1 Ga two-stage Nd and Pb model ages that imply a crustal origin (Fig. 3c; Table S3). These isotopic data overlap with both the known Proterozoic basement ($\varepsilon Nd_{(70\ Ma)}$ = 1.6 to -21.2), particularly the 1.1 Ga diabase dykes (Fig. 3b), and CPTZ garnet-clinopyroxene xenoliths. These xenoliths, equilibrated at pressures and temperatures (*P*–*T*) of ca. 1.0–2.8 GPa and 600–850°C[26], contain copper-bearing sulphides[25] and have been dated by U–Pb zircon at ca. 150 Ma and 75 Ma[26,27,28], yet their origins remain unclear. It is possible they originate from cumulate 'arclogites' derived from juvenile mantle-derived magmas[25,26,27,28]. Alternatively, they could represent Proterozoic-aged mafic lower crust[29,30] based on Nd, Pb and Re–Os mantle extraction ages spanning ca. 2.1–0.5 Ga[29,30] and unradiogenic Hf isotopes from their zircons[26] (Fig. 3d). Both I-type and S-type Laramide intrusions also show extensive zircon inheritance (Fig. 3c), with U–Pb dates of ca. 1.1, 1.4, 1.65, 1.7, 1.98 and 2.64 Ga[11,31]. The younger dates correlate with Yavapai-Mazatzal accretionary orogenesis at ca. 1.7–1.6 Ga[33], extensive Granite-Rhyolite Province magmatism at ca. 1.4 Ga and the large igneous province responsible for ca. 1.1 Ga[32] diabase dykes. These dates overlap with the model ages of Laramide granitoids (Fig. 3c) suggesting significant assimilation of Proterozoic crustal material.

Additional constraints can be inferred from exposures of the subducted Farallon plate at Cemetery Ridge and in the Plomosa Mountains (Fig. 2b). Here, the Orocopia and Pelona Schists equilibrated at *P*–*T* conditions of ca. 0.8 GPa and 660°C between ca. 75–65 Ma[34,35,36]. This subduction-zone metamorphism not only temporally and spatially overlaps with the zenith of Laramide granitic magmatism (and PCD formation) but also suggests that the leading edge of the Farallon flat-slab had been transported >500 km directly beneath North America (Fig. 1b). It is possible that this removed a substantial (~80 km) thickness of subcontinental lithospheric mantle beneath the Colorado Plateau[37,38].

Integration of these diverse observations suggests that the mantle wedge beneath the CPTZ was largely eliminated during the genesis of the Laramide granitoid magmas and associated PCDs. Isotope mixing calculations (Methods and Supplementary Material) support this hypothesis, revealing that Laramide granitoid magmas had to contain a significant proportion (>70–90%) of melt derived from various combinations of mafic and felsic Proterozoic crustal sources. From a metallogenic standpoint, it is noteworthy that this Proterozoic crust may have been pre-enriched in copper as suggested by the ca. 1.7 Ga Squaw Peak porphyry copper deposit[39] (Fig. 2b), the higher concentration of porphyry deposits within the Mazatzal terrane compared to the Yavapai and Mojave Terranes, and the presence of copper-bearing sulphides in the garnet-clinopyroxene xenoliths[25].

To provide further insight into the role of crustal anatexis in the formation of the Laramide Porphyry Province and potential sources of the Laramide granitic magmas, we constrain the thermal history and chronology of poorly-understood amphibolite-granulite facies metamorphic rocks exposed in the Harcurvar, Harquahala, and Granite Wash Mountains metamorphic core complexes[40,41,42,43,44,45,46,47] in central Arizona (Figs. 2b and 4), which collectively represent a 40 km thick section of exhumed CPTZ mid-lower crust[46,48]. These rocks provide direct evidence bearing on our model for magma generation during the Laramide orogen.

RESULTS

Field Relationships, Petrography and Thermobarometry

The Harcuvar, Harquahala, and Granite Wash Mountains (Figs. 2 and 4) are a series of metamorphic core complexes exhumed along the NE-verging Bullard-Eagle Eye extensional detachment fault between ca. 21–11 Ma[49,50]. Structurally beneath the extensional detachment, within the Granite Wash Mountains, a major SSW-verging Laramide-age contractional structure – the Hercules Thrust – is preserved[40,43]. The Hercules Thrust places Proterozoic basement over Mesozoic-Palaeozoic sedimentary rocks[40,43] and is cut by the ~79–70 Ma[42] S-type Tank Pass Granite and the ~78 Ma I-type Granite Wash Granodiorite[40] (Fig. 4b). A sample of mylonitized footwall metasediments (TLAZ22-167) displays a peak metamorphic assemblage of epidote-muscovite-biotite-titanite-quartz, which equilibrated at *P–T* conditions of 0.38 ± 0.05 GPa and 502 ± 25°C (Fig. 4b-c; Table S4). This assemblage is syn-kinematic with top-SSW shear on the thrust, suggesting compressional deformation was synchronous with regional metamorphism.

With increasing structural depth beneath the Hercules Thrust, metamorphic grade increases and kyanite-sillimanite-bearing schists, migmatites and amphibolites (representing metamorphosed Proterozoic basement and its cover) crop out in the Harcuvar Mountains (Figs. 4 and 5). Many of these lithologies display textures indicative of partial melting, including quartzo-feldspathic leucosomes (former melt) and biotite-rich melanosomes (restite) and also contain secondary copper and silver oxides (Supplementary Material). In places, leucosomes are complexly and ptygmatically folded (Fig. 5), suggesting melting occurred during contractional deformation, and can be traced from high melt-fraction domains to garnet-biotite-muscovite leucogranites that outcrop at structurally higher levels (e.g., Tank Pass and Browns Canyon Granites; Figs. 4 and 5).

In sample TLAZ22-08 (Harcuvar Mountains garnet-sillimanite migmatite), chemical traverses across garnet porphyroblasts (Table S5 and Supplementary Material) reveal flat, homogenized cores and resorbed rims indicating that the prograde growth history has been modified by high-temperature diffusion[51]. Garnet interior compositions are therefore interpreted to represent peak *P–T* conditions. Thermobarometric calculations and petrological modelling suggest the garnets equilibrated with plagioclase-K-feldspar-biotite-sillimanite-quartz-ilmenite-magnetite-melt at 0.75 ± 0.06

GPa and 780 ± 36 °C (~28 km depth; Fig. 4c and Table S4). The lack of primary muscovite and the presence of minor K-feldspar (Supplementary Material) is also consistent with conditions locally surpassing muscovite breakdown above the solidus[52,53]. Nevertheless, the low volumetric proportions of peritectic K-feldspar (3%) and sillimanite (1.8%) relative to melt (35%) differ from those expected from vapour-absent muscovite dehydration melting[50] (normally in a ratio 8:5:10). This requires anatexis to have occurred with 8–12 mol% H_2O (Supplementary Material) equating to ~2.4–3.5 wt% H_2O. This is significantly greater than the observed bulk rock composition from mineralogically bound water (4.3 mol% H_2O equating to ~1.2 wt% H_2O), necessitating ~3.7–7.7 mol% H_2O (~1.0–2.2 wt% H_2O) to be added to the rock during anatexis. At temperatures <700°C and 8–12 mol% H_2O (~2.4–3.5 wt% H_2O), a free fluid phase is expected, and water-saturated melting would have occurred (reaction 1):

1) Muscovite + Plagioclase + Quartz + H_2O = Sillimanite + Melt

However, at temperatures >700°C, H_2O remains as a free fluid phase only when there is a large excess of added water[52] (Supplementary Material). The addition of water is therefore buffered by the production of more (trondhjemitic) melt due to the consumption of plagioclase and does not drastically change the topology of muscovite breakdown[51] (Supplementary Material). Therefore, at peak conditions, melting is interpreted to have progressed by incongruent breakdown of muscovite (reaction 2):

2) Muscovite + Quartz + Plagioclase = Sillimanite + K-Feldspar + Melt

Constraints on the retrograde *P–T* history can be inferred from garnet rims in contact with biotite, matrix plagioclase, sillimanite, and secondary muscovite, which suggest cooling occurred at 0.65–0.75 GPa and 690–750°C (Fig. 4c and Supplementary Material). Titanium-in-biotite thermometry of ~600–680°C in sample TLAZ22-08 indicates that retrograde biotite growth occurred at sub-solidus conditions and, together with the occurrence of coarse, cross-cutting muscovite in sample TLAZ22-03 (Supplementary Material), suggests that hydration of the metamorphic rocks continued during melt crystallization. At higher structural levels along the southern edge of the Harcuvar Mountains, biotite-muscovite schists contain a penetrative foliation dipping steeply (~70°) towards the SSE and a NE-SW stretching lineation with top-NE kinematics (sample TLAZ22-03). Because this top-to-NE shear fabric cross-cuts the compressional features (Fig. 4a-b), it is interpreted to have formed during Miocene shearing on the extensional Bullard Detachment.

Rb–Sr Geochronology

Five samples (TLAZ22-03, TLAZ22-08, TLAZ22-167, TLAZ87 and TLCR-09) were dated by *in-situ* Rb–Sr analysis to constrain the timing of cooling and/or deformation (Table S6). White mica and plagioclase aligned with the top-SSW shear fabric in sample TLAZ22-167 (Hercules Thrust mylonite, Granite Wash Mountains) gave an

isochron date of 71.7 ± 12.9 Ma (MSWD = 5.3) that constrains the timing of thrusting and lower amphibolite-facies conditions. Plagioclase in sample TLAZ22-03 (Harcuvar Mountains biotite-muscovite schist) yielded a date of 64.0 ± 45.0 Ma (MSWD = 2.2), and K-feldspar and biotite from sample TLAZ87 (Harquahala Mountains migmatite) were dated at 45.3 ± 3.5 Ma (MSWD = 1.4). These dates overlap with existing K–Ar cooling ages spanning ca. 70–45 Ma[45,54] from metamorphic rocks at similar structural positions. Given that the 450–550°C closure temperature of the Rb–Sr isotope system in these minerals[55] is far below the peak metamorphic temperatures of 500–780°C, these data constrain anatexis to be equivalent to, or older than, ca. 72–45 Ma. In contrast, sample TLAZ22-08 (Harcuvar Mountains garnet-sillimanite migmatite) yielded a Rb–Sr age of 20.5 ± 2.2 Ma (MSWD = 0.9), and TLCR-09 (Orocopia Schist from Cemetery Ridge) an age of 26.0 ± 3.2 (MSWD = 2.2). These younger ages overlap with white mica and biotite Ar–Ar and zircon and apatite (U/Th)/He cooling ages from the region (21–11 Ma)[56,57,58], suggesting these samples experienced either: (1) delayed cooling in comparison to higher structural levels; (2) reheating during Basin and Range extension; and/or (3) isotopic resetting during deformation-induced recrystallisation.

U–Th–Pb Geochronology

Monazite grains from Harcuvar Mountains samples TLAZ22-03 (biotite-muscovite schist) and TLAZ22-08 (garnet-sillimanite migmatite) were analysed by *in-situ* laser ablation split-stream U–Th–Pb geochronology to constrain the timing of peak metamorphism (Fig. 5 and Table S7). Three distinct phases of monazite growth were identified at ~145 Ma, ~73–60 Ma, and ~20–15 Ma. Chemical data suggest that monazite dates falling between these age populations are physical mixtures of older and younger material, although it is possible that monazite growth and reprecipitation continued between 60–40 Ma evident in the younger tail of the ~73–60 Ma age population (Fig. 5).

Integration of our U–Th–Pb and Rb–Sr results with existing geochronology from the region suggests: (1) monazite growth at ~145 Ma reflects eastward migration of metamorphism during the Sevier Orogeny from a peak at ca. 167–158 Ma in the Funeral Mountains[59] and ca. 164–161 Ma in the Big Maria Mountains[60] (Fig. 2b); (2) monazite growth between ~73–60 Ma coincides with migmatite-related leucogranite crystallization at ~78–54 Ma in the adjacent Harcuvar, Harquahala, Mesquite, and Moon Mountains[40,47,61,62,63], shearing on the Hercules Thrust at ca. 72 Ma, granitic I- and S-type magmatism (78–54 Ma) and PCD formation (72–56 Ma); and (3) monazite growth between ~20–15 Ma occurred during Basin and Range extension[56,57,58] and does not reflect high-grade metamorphism. The evidence for this is two-fold. Firstly, this monazite considerably post-dates the recorded 72–45 Ma Rb–Sr ages which reflect moderate crustal temperatures of ~450–550°C[55], and secondly, these monazite domains are aligned with the cross-cutting shear fabrics that developed during core complex exhumation between ~21–11 Ma[56,57,58] suggesting that monazite grew due

to fluid-induced reprecipitation (Supplementary Material). We therefore interpret the timing of peak amphibolite-granulite facies metamorphism along the CPTZ to be ca. 73–60 Ma, although Rb–Sr and K–Ar cooling ages suggest temperatures >450–550°C persisted until ca. 45 Ma (Fig. 4).

DISCUSSION

Tectonic, Magmatic, and Metallogenic Implications

Our data indicate that crustal anatexis was a regional feature along the CPTZ between ca. 73–60 Ma and reached *P–T* conditions of at least ca. 0.75 GPa and 780°C (TLAZ22-08). This requires an overburden of ~28 km (Fig. 4c) and suggests the average geothermal gradient was ~28°C/km (Figs. 4c and 6). This would imply that during peak Laramide orogenesis: (1) supra-solidus temperatures occurred at depths >25 km; and (2) the CPTZ crust must have been at least ~50–60 km thick, based on the addition of the ~28 km overburden to the present-day Moho depth of ~25–30 km beneath central Arizona[64]. This is consistent with paleo-crustal thickness estimates derived from Sr/Y and La/Yb ratios of Laramide granitic rocks[65] and indicates the crust was thinned by a factor of two during subsequent Basin and Range extension. Notably, these findings argue against the traditional premise that Laramide shortening did not result in significant crustal thickening in Arizona[14,15]. We suggest this is because the thrust belt was significantly dismembered by Basin and Range extension and that many of the Laramide thrusts are not easily recognised or appreciated.

The timing of peak metamorphism and water-fluxed anatexis coincided with the onset of flat-slab subduction beneath the CPTZ, evidenced by the isotopic signature of Laramide magmatism (Fig. 3a) and the timing of dehydration reactions in the Farallon Plate between ca. 75–65 Ma[34,36] (Figs. 5–6). This was also contemporaneous with the formation of significant PCDs in Arizona (e.g., Bagdad at ca. 72 Ma[66]; Ray at ca. 72–68 Ma[11] and Resolution at ca. 64 Ma[11]; Figs. 2 and 5) and the end of contractional deformation (shearing on the Hercules Thrust at ca. 72 Ma). Integration of these geodynamic constraints with the “crustal” isotope composition of granitic rocks, Proterozoic model ages and potential pre-enrichment of copper in the Proterozoic basement[28,39] supports the hypothesis that Laramide granitoid magmatism and PCD genesis were largely a product of water-fluxed crustal anatexis during flat-slab subduction.

Since the timing of contractional deformation, anatexis (73–60 Ma), and porphyry genesis (73–56 Ma) in Arizona are temporally limited and progressively get younger towards the southeast (Fig. 2), it also suggests these phenomena are transient and diachronous. However, flat-slab subduction can explain these observations. This is because it would be expected to produce a diachronous thermal evolution of the overlying North American crust[67] due to the interplay between competing mechanisms: (1) increased tractions on the base of the North American plate or increased end-loading, leading to crustal thickening and resulting in heating with

characteristic timescales >10 Myr due to conductive relaxation of isotherms[68]; (2) shear heating along the plate interface (the Moho); (3) refrigeration or even heating due to underthrusting of the Farallon Plate (~660°C; Fig. 6c), depending on the initial crustal geotherm, age of the subducted oceanic lithosphere and the convergence rates; (4) remnant mantle wedge heat flow, depending on the lateral position in the crust relative to the geometrical position where the Farallon slab steepens into the asthenosphere; (5) heat flow from the earlier Sevier-related metamorphism and orogenesis (occurring at ca. 145 Ma). However, given reasonable geodynamic constraints, it is most likely that thermal climax and porphyry genesis at any given time, occurred in a geodynamic 'sweet-spot' immediately above the leading edge of the Farallon flat-slab that migrated through space and time during ongoing flat-slab subduction (Fig. 6).

At the 'sweetspot', elevated crustal temperatures would have prevailed due to the proximity to the laterally displaced mantle wedge, in combination with thickened crust. Volatiles derived from the dehydrating flat-slab could also pass straight into the overlying crust, facilitating melting of Proterozoic lower crustal rocks, which were probably already dehydrated. This crustal hydration/melting process may have also caused rheological weakening, causing the locus of contractional deformation to migrate further inboard in front of the leading edge of the Farallon flat-slab. However, on longer timescales (>15 Myrs), the continual underthrusting of the Farallon flat-slab likely caused cooling of the overlying North American crust[67], as evidenced by our Rb–Sr cooling ages spanning ca. 45–20 Ma. This diachronous migrating 'sweet-spot' can potentially explain why the locus of magmatism, deformation and metamorphism swept from SW to NE across Western USA throughout the Late Cretaceous and Palaeocene as the Farallon Plate advanced towards the NE. It can also elegantly explain the systematic spatial-temporal mineralization relationships involving: 1) pre-mineralization volcanism, compression and barren I-type granitic magmatism related to steep subduction and arc magmatism prior to flat-slab subduction (inboard from the 'sweetspot'), (2) syn-mineralization I- and S-type granitic magmatism and crustal anatexis coinciding with the ending of compression during the initial stages of flat-slab subduction (close proximity to the 'sweet-spot'), and (3) post-mineralization barren S-type magmatism, localized extensional deformation and cooling due to continued underthrusting of the Farallon Plate after the 'sweet-spot' has passed (Fig. 6).

Tectonic and Metallogenic Model

We propose that I-type granitic magmas associated with most Laramide PCDs were derived from melting mafic (amphibolitic or garnet pyroxenite) lower crustal protoliths, originally extracted from the mantle at ca. 1.7–1.1 Ga (Fig. 3c). This is supported by: (1) the unradiogenic Nd isotopic and zircon inheritance data which overlaps with the Proterozoic basement; and (2) interpreting the CPTZ sulphide-rich[25] garnet-clinopyroxene xenoliths as Proterozoic aged lower crustal granulites that experienced both high-grade Sevier and Laramide metamorphism. This latter interpretation is

consistent with the xenolith model ages (ca. 2.1–0.5 Ga[29,30,69]), and U–Pb zircon dates (ca. 75 Ma and ca. 150 Ma)[26,27,28] which overlap with our Laramide and Sevier metamorphic monazite dates (Fig. 5). Alternatively, if the ca. 75 Ma and ca. 150 Ma U–Pb zircon dates in the garnet-pyroxenites are magmatic, it would suggest these xenoliths are 'arclogite' cumulates that crystallized during earlier phases of arc related magmatism prior to flat-slab subduction and PCD genesis (Fig. 5). However, remelting this sulphide rich source[26] would be expected to form copper enriched magma with isotopically juvenile signatures, in disagreement with the Nd and Pb data[29,30,69].

Although dehydration melting of amphibolite (or granulite) is expected to produce I-type granitic magmas, the high solidus temperatures and low melt volumes and water contents (<2 wt% H_2O)[5] of such magmas are unlikely to form extensive magmatic-hydrothermal systems in the shallow crust. However, volatiles derived from the subducting flat-slab can migrate directly across the Moho and into the overlying crust (Figs. 6b). In Arizona, hydration of the lower crust is supported by: (1) the requirement for externally derived water during anatexis in the Harcuvar Mountains; (2) the presence of metasomatized gneisses structurally above the Orocopia Schists at Cemetery Ridge[36]; and (3) cross-cutting amphibole growth in the garnet-clinopyroxene xenoliths[26]. Given a crustal geothermal gradient of ~28°C/km, temperatures would have exceeded the water-saturated solidus (~650°C) at depths >25 km (Fig. 6c). Water-saturated melting of mafic lithologies at similar depths has been demonstrated to produce: (1) water-rich melt (>8 wt% H_2O)[70]; (2) larger melt-fractions (locally >50% volume melt)[70]; (3) peraluminous magma with enrichment in Ca and Al and relative depletion in Fe, Mg, Ti and K[70,71,72]; (4) an increase in amphibole stability as a restitic phase and preferential consumption of plagioclase during anatexis[70,71,72]; and (5) magma enriched in Sr and depleted in Ba[52]. Such crustal derived melts would also have 'adakite-like' chemistries characterised by elevated Sr/Y, La/Yb and (Eu/Eu*)/Yb ratios[5,73], as observed in many Laramide porphyry intrusions[71,72].

In contrast, the S-type granitic rocks show variable, but sometimes significant ore-forming potential (e.g., Diamond Joe and Texas Canyon). Because these rocks contain garnet-muscovite-biotite-magnetite and display similar unradiogenic isotopic signatures and zircon inheritance, we infer they were derived from Proterozoic sedimentary protoliths, potentially the weathered products of the ca. 1.7–1.4 Ga granitic basement, which was re-buried during Laramide or earlier orogenesis. Vapour-absent dehydration melting of this source would be expected to form more metaluminous magma[52,53] with lower volatile contents and presumably limited ore-forming potential. In contrast, water-fluxed anatexis would favour the formation of oxidized, volatile-rich, and strongly peraluminous magma[52] with elevated fertility indices (Sr/Y and (Eu/Eu*)/Yb)[73], due to consumption of plagioclase during anatexis[52].

We conclude that flat-slab subduction was fundamental to the formation of the Laramide Porphyry Province as it allowed volatiles to flux directly into the lower crust, which may have been heterogeneously pre-enriched in metals, and caused anatexis with the potential to form fertile porphyry magma. This occurred above the location of

a diachronously migrating geodynamic “sweet-spot” that represented the leading edge of the Farallon flat-slab (Fig. 6). It is possible that other convergent plate boundaries that experienced flat-slab regimes, underwent a similar mechanism of volatile mediated crustal anatexis of pre-cursor igneous rocks. This may explain the correlation between flat-slab subduction and PCD genesis in the Southwest USA, Central Andes, Southeast China, and Southern Tibet that collectively host >50% of the world’s known reserve[9]. We therefore propose such flat-slab settings to be favourable exploration targets to meet society’s ever-increasing demand for copper.

METHODS

Electron Probe Micro-Analysis (EPMA)

The compositions of phases in samples TLAZ22-08 and TLAZ22-167 were derived from electron probe micro-analysis (EPMA) that were performed on a CAMECA SX100 electron microprobe at the Department of Earth Sciences, University of Bristol. Operating conditions involved an accelerating voltage of 15.0 keV corresponding to a current of 20 nA, a range of primary standards were used including andradite (Fe, Mg, Ca), TiO_2 (Ti), Mn metal (Mn), labradorite (Na, Al, Si) and sanidine (K) for major elements and secondary standards include Diopside, KK1, SPH Labradorite, RN18 and FDLA1. Garnet line profiles were collected using a 75-micron step size across all garnets from sample TLAZ22-08 corresponding to between 25 and 30 analyses per porphyroblast. Garnets show minor zoning in major elements, with homogenous cores and resorbed rims (Supplementary Material). Pyrope (Prp) [XMg] displays convex down trends (0.18-0.13) from core to outer rim, grossular (Grs) [XCa] remains either homogenous or increases towards the outer rim (0.05-0.07), whereas almandine (Alm) [XFe] remains homogenous before decreasing towards the outer rim (0.73-0.71). However, spessartine (Spss) [XMn] is homogeneous or concaves upward (0.05-0.08) from core to rim. Mineral abbreviations follow the guidelines of Whitney and Evans (2010)[74]. Anhydrous phase compositions were calculated to standard numbers of oxygen per formula unit[75], micas were recalculated to 11 oxygens, and chlorite to 28 oxygens. Where present, H_2O content was assumed to occur in stoichiometric amounts. The proportion of Fe^{3+}/Fe_{total} was calculated using AX[76]. The complete EPMA database is presented in Supplementary Table S5.

Thermobarometry and Petrological Modelling

Several thermobarometric approaches were employed to constrain the *P-T* conditions of metamorphism, including the Ti-in-biotite thermometer[77], the garnet-biotite thermometer[77], the garnet–aluminosilicate–plagioclase–quartz (GASP) barometer[78,79] the garnet-muscovite-plagioclase (GMP) barometer, and Average *P-T*[80] using THERMOCALC version TC-3.50i with characteristic end members judged to be in textural equilibrium for each sample. The complete results are presented in Table S4.

Phase diagram construction was performed using THERMOCALC version TC-350i and Theriak Domino[81] and the internally consistent thermodynamic data set ds62[82]. Migmatite sample TLAZ22-08 was modelled in the 11-component system MnO–Na_2O–CaO–K_2O–FeO–MgO-Al_2O_3–SiO_2–H_2O–TiO_2–O (MnNCKFMASHTO). The a–x relations for solid-solution phases were used: clinopyroxene (diopside–omphacite–jadeite) and clinoamphibole (glaucophane–actinolite–hornblende)[83]; garnet, biotite, muscovite–paragonite, and chlorite; epidote; ilmenite[84] and plagioclase feldspar[85]. Pure phases comprised talc, lawsonite, kyanite, sillimanite, andalusite, zoisite, quartz, coesite, and rutile. The effective bulk composition for sample TLAZ22-08 were calculated using mineral proportions derived by point counted analyses of an entire thin section using J-microvision and representative EPMA-derived phase compositions following the method of ref. 86. Details on the determination of the bulk-rock composition used to perform phase equilibrium modelling are shown in the Supplementary Material. Uncertainties related to the absolute positions of assemblage field boundaries calculated phase diagrams have been shown to be less than ± 0.1 GPa and ± 50 °C at the 2σ (95% confidence) level[80,85], with this variation being largely a function of propagated uncertainty on end-member thermodynamic properties within the data set. However, because phase diagrams were calculated using the same dataset and a–x relations, it has also been shown that similar absolute errors associated with dataset end-members cancel, and calculated phase equilibria are relatively accurate to within ± 0.02 GPa and ± 10–15°C[82,87]. In melting calculations, the bulk-rock suprasolidus water content of sample TAZ22-08 was varied to investigate the effect of water fluxed melting. In a closed system scenario, the bulk-rock suprasolidus water content was fixed in order to allow minimal fluid saturation at the wet solidus, here defined as ~1 mol% free H_2O. It was determined 7 mol% H_2O represents fluid saturation at the wet solidus. Bulk rock H_2O content was estimated at 4.5 mol% determined by combining point counted volume estimates of hydrous phases and average phase compositions (Supplementary Material). The *P*–*T* conditions of peak metamorphism were determined by investigating compositional isopleths for pyrope and grossular content in garnet. Since these isopleths vary to first order with changes in pressure and temperature and commonly intersect at high angles, they specify unique intersection points with a high degree of confidence for tracking garnet composition evolution in *P*–*T* space. The intersections of isopleths representing measured compositions are represented by shaded boxes indicating uncertainties at the 1s level calculated by THERMOCALC/Theriak Domino. The results were verified by comparing mineral volumetrically determined mineral proportions by point counting using J-microvision and intersection of garnet compositional isopleths against those predicted by the petrological model. The results are in good agreement with conventional thermobarometry. Temperature-Molar % (H_2O) calculations were performed to test the effect of an open system to simulate water fluxed melting (Supplementary Material). Calculations were performed between 4 mol% H_2O and 20 mol% H_2O, the former representing a closed system with water derived from hydrous phases in the rocks such as biotite and muscovite, the later representing an open system and fluxing water from an external source. Intersection

of mineral volume isopleths were used to constrain the range of water contents, and the position of k-feldspar out reaction defines the maximum possible amount of water that anatexis occurred under. The full results are presented in the Supplementary Material and discussed in the Main Text.

Sr-Nd Isotopes and Sm-Nd Model Ages

$^{87}Sr/^{86}Sr$ and $^{143}Nd/^{144}Nd$ measurements were compiled from the literature for Arizona Laramide I-type and S-type granitoids, PCDs, Laramide volcanics, xenoliths and basement. Initial Sr and Nd isotope ratios were calculated using the available U–Pb magmatic ages or K–Ar ages and decay constants of $1.393*10e^{-11}$ for ^{87}Sr and $6.524*10e^{-12}$ for $^{147}Sm^{87}$. Initial Sr isotope values are quoted as $^{87}Sr/^{86}Sr_{(i)}$ and Nd isotope values are quoted as $\varepsilon Nd_{(t)}$ using the CHUR values of ref.89. Two-stage Nd model ages were calculated using $^{147}Sm/^{144}Nd$ of 0.09 and 0.12, that of average evolved and less evolved continental crust[90] respectively, and a depleted mantle with a modern-day $^{143}Nd/^{144}Nd$ of 0.51315 and $^{147}Sm/^{144}Nd$ of 0.2135[91]. Two component Sr–Nd mixing calculations were performed between a depleted mantle source and a nominal crustal source, the latter was varied to reflect a mixture of the average felsic crust and mafic crust from Arizona and 20 different combinations were used representing 5% sequential additions of mafic and felsic crust. The resultant calculated mixtures between depleted mantle and ‘mixed’ crust that were deemed successful plotted within the 95% confidence ellipse for the I-type granites and the successful results were plotted up as a cumulative density plot to show the statistical likelihood of the relative importance of crustal and mantle sources. The results are compiled with source references in Table S3 and the Supplementary Material and strongly suggests that the PCD data can be explained by various combinations of different (crustal) source components, although we cannot entirely rule out a juvenile mantle derived component, it is likely this component has to be relatively small.

Rb–Sr Geochronology

The analytical procedure for the in situ Rb–Sr dating presented in this study is extremely similar to that described in Ref.92. The *in-situ* Rb–Sr dating of samples was conducted using a 193nm Photon Machines excimer laser equipped with ARIS[93] (aerosol rapid introduction system). Laser operating conditions, which were standardised for dating, were a 110 µm laser spot diameter, which was ablated using a repetition rate of 10 Hz, and a fluence of 7 J cm^{-2} for 600 laser pulses. These spots were positioned to target identified phases of interest which include feldspar and mica which were exposed on polished surfaces of cut billets. This laser ablation system was coupled with Proteus, a collision cell – multicollector – inductively coupled plasma tandem mass spectrometer (CC-MC-ICPMS/MS) housed at the University of Bristol. To provide chemical resolution of Rb^+ and Sr^+ during analysis[94,95] a reaction gas mixture consisting of 5% SF_6 (99.99% purity) in He (99.9999%) was used. The flow

rate for the He and SF_6 collision cell gases was 2 ml min^{-1} and 0.025 ml min^{-1} respectively. During analysis the SrF isotopologues ($^{86}SrF^+$, $^{87}SrF^+$ and $^{88}SrF^+$) and atomic $^{85}Rb^+$ and $^{88}Sr^+$ were collected for each spot. The measurement of fluorinated and monoatomic ion species was achieved by adjusting the centre mass of the sector magnetic field of Proteus during analysis. The position of the faraday cup collectors, integration and idle times were identical to those specified in Ref.92. However, in this method $10^{13}\,\Omega$ resistors were used in the collection of $^{87}SrF^+$ and $^{86}SrF^+$ ions to improve signal to noise ratio during collection, and thus improve $^{87}SrF/^{86}SrF$ precision for small ion beam sizes[95,96,97]. The remaining isotopes, $^{88}SrF^+$, $^{88}Sr^+$, and $^{85}Rb^+$ were collected in faraday cups which were matched with $10^{11}\,\Omega$ resistors. To correct for the slower response time of the $10^{13}\,\Omega$ resistors, relative to $10^{11}\,\Omega$ resistors, a conventional tau correction method was used[96]. Mean radiogenic Sr isotope ratio $^{87}Sr/^{86}Sr$ for each spot analysis was calculated using the measured $^{87}SrF^+/^{86}SrF^+$ and $^{88}SrF^+/^{86}SrF^+$ to correct for natural and instrumental mass dependent fractionation by use of an exponential law correction. Residual inaccuracy after the exponential law correction was externally normalised using well characterised in-house feldspar standard Te-1[92], which was analysed every ~10 sample analyses. Sample analyses which were beyond the mean $^{88}SrF^+/^{86}SrF^+$ ratio ± 2σ uncertainty measured for Te-1 were excluded due to the presence of an isobaric interference on $^{86}SrF^+$.

Mean sample $^{87}Rb/^{86}Sr$ ratios for each spot analysis was converted using measured $^{85}Rb^+/^{88}SrF^+$ ratios, which were externally normalised to analysis of NIST SRM 610 glass and a $^{87}Rb/^{86}Sr$ ratio of 2.389[91]. Correlation coefficients were also calculated for measured $^{85}Rb^+/^{88}SrF^+$ and $^{87}SrF^+/^{86}SrF^+$ ratios. Differential Rb–Sr elemental fractionation of the NIST SRM 610 glass standard and sample minerals was corrected for the analytical session using the Dartmoor Granite (DG-1) as a secondary standard[98]. An $^{87}Rb/^{86}Sr$ correction factor of 0.952 ± 0.011 was determined from the analysis of plagioclase feldspar, K-feldspar and biotite in DG-1. This single correction factor was applied to all calculated sample feldspar and mica $^{87}Rb/^{86}Sr$ ratios in this study.

Rb–Sr ages, initial radiogenic Sr isotope ratios and uncertainties were all calculated using the open access software package IsoplotR[99] using input mean calculated $^{87}Rb/^{86}Sr$, $^{87}Sr/^{86}Sr$ ratios with associated 2σ uncertainties and correlation coefficient values. Total age uncertainties were then calculated by accounting for the relative uncertainty of sample isochron slope calculated in IsoplotR[99] and the relative uncertainty of the DG-1 isochron slope used for calculation of the $^{87}Rb/^{86}Sr$ correction factor[93]. The full results are presented in Table S6.

U–Th–Pb Geochronology

In-situ LA-ICP-MS U–Th–Pb split-stream geochronology was conducted at the Geochronology and Tracers Facility, British Geological Survey (Nottingham). The U–

Th–Pb measurements were collected on a Nu Instruments Attom single-collector ICP-MS following similar analytical conditions and measurement protocols to those described previously[100], with detailed methodology provided in the supplementary text. Laser conditions were a 14 µm spot size, 10 Hz repetition rate, 17 seconds of ablation using a fluence of 3.1 J cm^{-2}. The He carrier gas was split after exiting the laser and sent to both the SC-ICP-MS for U–Th–Pb, and to an Agilent 7500 quadrupole ICP-MS for measurement of trace elements. The full analytical conditions for both instruments are provided in Table S7. Matrix-matched normalisation using standard sample bracketing was used for U–Th–Pb geochronology and trace elements, with data reduction for geochronology comprising the Attolab TRA software and in-house spreadsheet, and Iolite4[101] for trace elements. Monazites 44069[102] and Bananeira[103] were used as primary reference materials for normalisation of U–Th–Pb and trace elements, respectively. Internal standardisation of trace elements used ^{31}P assuming 22.45 wt%. All plotting and age calculations were conducted with IsoplotR[98] and are shown and quoted at 2σ.

Acknowledgements

This work was supported by generous funding from BHP. We would like to thank Noah Metz, Stephen Alizadeh, Liz Dunlop, Joel Leonard, Peter Loader, Hero Bain, and Eliana Toro Paz for assistance in the field. Robert Loucks is thanked for highly constructive discussion and providing the initial igneous geochemical database. We would like to add thanks for discussions and constructive comments from Alison Rust, Matthew Jackson, Brian Tattitch, Steffen Hagemann, Giulia Consuma, Richard Brooker, Bob Myhill, Richard Palin, Andrew Smye, and Chris Hawksworth. Finally, we thank Benjamin Buse, Anthony Oldridge and Jeremy Rushton for technical assistance.

Figures

Figure 1: Contrasting models for the formation of porphyry copper deposits (modified from Wilkinson, 2013)[1]. A) 'Standard' steep slab subduction with magmatic arc and porphyry copper deposits sourced from mantle wedge-derived melts[1]. B) Flat-slab subduction analogous to subduction of the Farallon plate during the Laramide Orogeny. Here, forced flow into the mantle wedge is cut off and volatiles derived from the slab (H_2O, CO_2, Cl, and S) pass straight into the base of the crust, triggering crustal anatexis, granitic magmatism, and potentially porphyry deposit formation.

Figure 2: A) Tectonic setting of porphyry copper deposits in the western USA[13, 104,105,106]. CPTZ = Colorado Plateau Transition Zone. B) Simplified geological map of Arizona showing the location of I-type and S-type granites, metamorphic rocks, Proterozoic basement granitoids and key structural features (thrust faults, high and low angle normal faults and monoclines). Porphyry copper deposits (PCDs) are represented by circles scaled according to economic value; see Supplementary Table

S2). Ages in blue reflect approximate constraints on the end of Laramide shortening based on (described in Supplementary Table S3). C) Sr/Y vs age (Ma) and D) Sr/Y vs (Eu/Eu*)/Yb for Laramide volcanic rocks, I-type and S-type granitoids. Sr/Y>35 and (Eu/Eu*)/Yb>2 indicate fertile porphyry magma[5]. The full suite of geochemical data is presented in Supplementary Table S4.

Figure 3: A) A compilation of Nd isotopes from igneous rocks from southwest USA and northwest Mexico that formed between 140 Ma and present day, highlighting the influence of Farallon flat-slab subduction between ca. 80–40 Ma on magma petrogenesis. Range of calculated basement εNd(t) over this period in the shaded domains, with more radiogenic values representing mafic younger (ca. 1.1 Ga) lithologies such as the diabase dikes, Grt-Cpx xenoliths and amphibolites and unradiogenic values representing felsic older (ca. 1.4–2.0 Ga) lithologies including the Proterozoic Granites and Pinal Schist. B) Summary of whole rock Sr–Nd isotopes for I-type and S-type granites, PCDs and basement lithologies compiled from sources described in Supplementary Table S4. Negative εNd(t) suggest all granitoids have unradiogenic signatures and overlap with the ca. 1.1 Ga diabase dikes, CPTZ xenoliths and Proterozoic basement. They are notably distinct from the juvenile mantle wedge-derived magmas. C) Whole rock two-stage Sm–Nd model age probability density plot for Laramide I-type granites (red), S-type granites (yellow), xenoliths (purple), basement (green) and zircon inheritance (grey), suggesting all granites have Proterozoic crustal sources. D) A compilation of Hf-in-zircon isotopes from granitic rocks from the southwest USA and northwest Mexico the I-type and S-type granitoids and CPTZ garnet-clinopyroxene xenoliths have overlapping unradiogenic isotopic signatures.

Figure 4. A) Study area map and sample locations in the Harcuvar, Harquahala and Granite Wash Mountains metamorphic core complexes and exposures of the Farallon Plate at Cemetery Ridge after ref. 40. B) Schematic cross section through the Harcuvar and Granite Wash Mountains showing the key structural relationships of: i) the Hercules Thrust being folded and cross-cut by the ca. 79 Ma Granite Wash Granodiorite and ca. 78–70 Ma Tank Pass Granite, ii) metamorphic grade increasing with increasing structural depth beneath the Hercules Thrust and iii) the extensional Bullard detachment cross-cutting the older compressional features. C) Summary *P–T–t* evolution of Laramide-age metamorphic rocks and migmatites in central Arizona. Shaded coloured polygons represent constraints from petrological modelling, shaded coloured ellipses represent average *P-T* results with 2σ uncertainties and green data points represent GASP and garnet-biotite thermobarometry results with 2σ uncertainties. Calculated temperature range from Ti-in-biotite thermometry in the light gay shaded box and Rb-Sr closure temperature range[55] in the gray zone. Peak metamorphic conditions of ca. 0.75 GPa and 750–780°C for sample TLAZ22-08 and

0.38 GPa and 502°C for sample TLAZ22-167 define a geothermal gradient of ~28°C/km between ca. 73 and 60 Ma.

Figure 5: Left Column: Schematic crustal section of Arizona and corresponding field photographs showing the following exposures: A) the upper crustal fold-thrust belt and porphyry copper deposits (e.g., Superior/Globe-Miami/San Pedro Valley), B) upper-mid-crustal S-type granites and low-grade metamorphic rocks (e.g. Santa Catalina Mountains), C) mid-lower crustal high-grade metamorphic rocks and migmatites (e.g., Harcuvar and Harquahala Mountains), D) lower crustal garnet-clinopyroxene xenoliths (e.g. Chino Valley), accreted pieces of the Farallon slab (Orocopia Schist), and E) subduction interface of the Farallon Plate (e.g. minor serpentinized peridotites and Orocopia Schists at Cemetery Ridge). Right Column: Probability density function plots showing a strong correlation between Laramide orogenesis and anatexis, the zenith of granitic magmatism and porphyry genesis, and metamorphism of the subducted Farallon slab. (i) published zircon U–Pb and molybdenite Re–Os ages from igneous rocks associated with porphyry copper deposits (Table S1); (ii) U-Pb zircon and K–Ar ages of I-type and S-type granites and volcanics (Table S1); and (iii) metamorphic U–Pb monazite ages from the Harcuvar Mountains (this study) and published zircon U–Pb ages from the Orocopia Schist at Cemetery Ridge, Plomosa Mountains[34,35], and garnet-clinopyroxene xenoliths[27].

Figure 6: Sequential Laramide porphyry copper deposit model for flat-slab subduction in Arizona showing the transition from a steep-slab to a flat-slab geometry and evolution of the geothermal gradient through time, with labels (i), (ii) and (iii) representing particle positions within the Farallon slab through time. A) Early Laramide orogenesis (85–75 Ma) is associated with steep subduction and arc magmatism/volcanism in western Arizona and California. B) During peak Laramide orogenesis (75–55 Ma), flat-slab subduction shuts off the mantle wedge, resulting in the termination of arc volcanism and increased tractions on the base of the plate causing crustal thickening and anatexis. C) Thermal profile of Laramide crust at ~75–55 Ma showing the location of Farallon slab dehydration and zone of supra-solidus temperatures causing crustal anatexis. D) *P–T* diagram showing the calculated Laramide geothermal gradient, conditions of crustal anatexis, and lowering of the solidus temperature by fluxing in external water. Geological features: (1) Orocopia Schist (Farallon Plate) ~0.8 GPa and 660°C ~70–65 Ma; (2) Hercules Thrust (top-SSW) ~85–71 Ma; (3) Harcuvar and Harquahala mountains migmatites ~0.75 GPa and 750–780°C ~73–60 Ma; (4) Tank Pass & Browns Canyon S-type granites (cuts Hercules Thrust) ~79–70 Ma; (5) NW Arizona PCDs ~73–68 Ma (Bagdad, Mineral Park, Diamond Joe, Copper Basin, Crown King); (6) Coyote Mountains Pan-Tak S-type granite ~58 Ma which intruded syn-Baboquivari Thrusting (top-ENE); (7) SE Arizona PCDs ~72–56 Ma (e.g., Ray, Resolution, Globe-Miami, San Manuel, Copper

Creek, Sierra Rita, Texas Canyon, Morenci & Safford); (8) Galiuro Mountains Thrusts (top-ENE) ~73–60 Ma; (9) Santa Catalina mountains Wilderness & Pinaleño S-type granites ~58–50 Ma; (10) 'Maricopa Thrust' syn-Wilderness S-type granites (top-WSW) ~58–50 Ma; (11) Water-saturated melting of ca. 1.7–1.1 Ga mafic lower crustal source between 75–55 Ma; (12) CPTZ garnet-clinopyroxene xenoliths ~150 Ma & 75 Ma.

REFERENCES

[1]Wilkinson, J., (2013). Triggers for the formation of porphyry ore deposits in magmatic arcs. *Nature Geoscience,* v. 6**,** p. 917–925 (2013). https://doi.org/10.1038/ngeo1940

[2]Park, J. W., Campbell, I. H., Chiaradia, M., Hao, H., and Lee, C. T., (2021). Crustal magmatic controls on the formation of porphyry copper deposit, *Nature Reviews Earth and Environment,* v. 2, p. 542–557 (2021). https://doi.org/10.1038/s43017-021-00182-8 v. 2(8), p. 542–557.

[3]Lee, C.T., and Tang, M., (2020). How to make porphyry copper deposits, *Earth and Planetary Science Letters*, v. 529, p. 115868, https://doi.org/10.1016/j.epsl.2019.115868.

[4]Richards, J. P., (2022). Porphyry copper deposit formation in arcs: What are the odds?. *Geosphere*, v. 18(1), p. 130-155.

[5]Loucks, R., (2021). Deep entrapment of buoyant magmas by orogenic tectonic stress: Its role in producing continental crust, adakites, and porphyry copper deposits, *Earth-Science Reviews*, v. 220, p. 103744, https://doi.org/10.1016/j.earscirev.2021.103744.

[6]Kay, S. M., and Mpodozis, C., (2001). Central Andean ore deposits linked to evolving shallow subduction systems and thickening crust. *GSA today*, March 2001, p. 4-9.

[7]Barton, M.D., (1996). Granitic magmatism and metallogeny of southwestern North America, in Brown, M., Candela, P.A., Peck, D.L., Stephens, W.E., Walker, R.J., and Zen, E., eds., The Third Hutton Symposium on the Origin of Granites and Related Rocks: *Transactions of the Royal Society of Edinburgh: Earth Sciences*, v. 87, and *Geological Society of America Special Paper* v. 315, p. 261–280.

[8]Schepers, G., van Hinsbergen, D., Spakman, W., Kosters, M. E., Boschmann, L. M., and McQuarrie, N., (2017). South-American plate advance and forced Andean trench retreat as drivers for transient flat subduction episodes. *Nature Communications*, v. 8, p. 15249. https://doi.org/10.1038/ncomms15249

[9]Leveille, R. A., and Stegen, R. J., (2012). The southwestern North America porphyry copper province. In Geology and Genesis of Major Copper Deposits and Districts of the World: A Tribute to Richard H. Sillitoe. *Special publications of the society of economic geologists*, Hedenquist, J. W., Harris, M., and Camus, F., v. 16 https://doi.org/10.5382/SP.16

[10]Liu, L., Gurnis, M., Seton, M., Saleeby, J., Müller, R. D., and Jackson, J. M., (2010). The role of oceanic plateau subduction in the Laramide orogeny. *Nature Geoscience*, v. 3(5), p. 353-357.

[11]Seedorff, E., Barton, M.D., Gehrels, G.E., Valencia, V.A., Johnson, D.A., Maher, D.J., Stavast, W.J.A., and Marsh, T.M., (2019b). Temporal evolution of the Laramide arc: U-Pb geochronology of plutons associated with porphyry copper mineralization in east-central Arizona, in Pearthree, P.A., ed., Geologic Excursions in Southwestern North America: *Geological Society of America Field Guide,* v. 55 , p. 369–400, https://doi.org/10.1130/2019.0055(15).

[12]Greig, R. E., and Barton, M. D., (2019). Regional-scale evolution of the Laramide arc and porphyry copper province, southwestern North America. *Geological Society of America Field Guide*, v. 55, p. 401-406. https://doi.org/10.1130/2019.0055(16)

[13]Hildenbrand, T. G., Berger, B., Jachens, R. C., and Ludington, S., (2000). Regional crustal structures and their relationship to the distribution of ore deposits in the western United States, based on magnetic and gravity data. *Economic Geology*, v. 95(8), p. 1583-1603.

[14]Favorito, D.A., and Seedorff, E., (2018). Discovery of major basement-cored uplifts in the northern Galiuro Mountains, southeastern Arizona: Implications for regional Laramide deformation style and structural evolution: *Tectonics*, v. 37, p. 3916–3940, https://doi.org/10.1029/2018TC005180.

[15]Seedorff, E., Richardson, C.A., Favorito, D.A., Barton, M.D., and Greig, R.E., (2019a). Crustal shortening and porphyry copper mineralization in the Laramide arc and superimposed extension: Introduction and themes, in Pearthree, P.A., ed., Geologic Excursions in Southwestern North America: *Geological Society of America Field Guide* v. 55 , p. 319–335, https://doi.org/10.1130/2019.0055(13).

[16]Favorito, D.A., and Seedorff, E., (2020). Laramide uplift near the Ray and Resolution porphyry copper deposits, southeastern Arizona: Insights into regional shortening style, magnitude of uplift, and implications for exploration: *Economic Geology*, v. 115, p. 153–175, https://doi.org/10.5382/econgeo.4697.

[17]Farmer, G. L., and Depaolo, D. J., (1984). Origin of Mesozoic and Tertiary granite in the western United States and implications for Pre-Mesozoic crustal structure: 2. Nd and Sr isotopic studies of unmineralized and Cu- and Mo-mineralized granite in the Precambrian Craton, *Journal of Geophysical Research*, v. 89(B12), p. 10141–10160, doi:10.1029/JB089iB12p10141.

[18]Lang, J. R., and Titley, S. R., (1998). Isotopic and geochemical characteristics of Laramide magmatic systems in Arizona and implications for the genesis of porphyry copper deposits*. Economic Geology*, v. 93(2), p. 138-170.

[19]Bouse, R. M., Ruiz, J., Titley, S. R., Tosdal, R. M., and Wooden, J. L., (1999). Lead isotope compositions of Late Cretaceous and early Tertiary igneous rocks and sulfide

minerals in Arizona: Implications for the sources of plutons and metals in porphyry copper deposits. *Economic Geology*, v. 94(2), p. 211-244. https://doi.org/10.2113/gsecongeo.94.2.211

[20]Fornash, K.F., Patchett, P.J., Gehrels, G.E., and Spencer, J.E., (2013). Evolution of granitoids in the Catalina metamorphic core complex, southeastern Arizona: U-Pb, Nd, and Hf isotopic constraints, *Contributions to Mineralogy and Petrology*, v. 165, p. 1295–1310, https://doi.org/10.1007/s00410-013-0859-4.

[21]Scoggin, S. H., Chapman, J. B., Shields, J. E., Trzinski, A. E., and Ducea, M. N., (2021). Early Paleogene Magmatism in the Pinaleño Mountains, Arizona: Evidence for Crustal Melting of Diverse Basement Assemblages during the Laramide Orogeny. *Journal of Petrology*, v. 62(12), egab095.

[22]Gottardi, R., McAleer, R., Casale, G., Borel, M., Iriondo, A., and Jepson, G., (2020). Exhumation of the Coyote Mountains metamorphic core complex (Arizona): Implications for orogenic collapse of the southern North American Cordillera. *Tectonics*, v. 39, e2019TC006050. https://doi.org/10.1029/2019TC006050

[23]Chapman, J., Runyon, S. E., Shields, J. E., Lawler, B. L., Pridmore, C. J., Scoggin, S. H., Swaim, N. T., Trzinski, A. E., Wiley, H. N., Barth, A. P., and Haxel, G. B., (2021). The North American Cordilleran Anatectic Belt, *Earth-Science Reviews*, v. 215, p. 103576, https://doi.org/10.1016/j.earscirev.2021.103576.

[24]Chapman, J. B., Dafov, M. N., Gehrels, G., Ducea, M. N., Valley, J. W., and Ishida, A. (2018). Lithospheric architecture and tectonic evolution of the southwestern US Cordillera: Constraints from zircon Hf and O isotopic data. *GSA Bulletin*, v. 130(11-12), p. 2031-2046.

[25]Chen, K., Tang, M., Lee, C. T. A., Wang, Z., Zou, Z., Hu, Z., and Liu, Y., (2020). Sulfide-bearing cumulates in deep continental arcs: The missing copper reservoir. *Earth and Planetary Science Letters*, v. 531, p. 115971.

[26]Rautela, O., Chapman, A. D., Shields, J. E., Ducea, M. N., Lee, C. T., Jiang, H., and Saleeby, J. (2020). In search for the missing arc root of the Southern California Batholith: PTt evolution of upper mantle xenoliths of the Colorado Plateau Transition Zone. *Earth and Planetary Science Letters*, v. 547, p. 116447.

[27]Chapman, A. D., Rautela, O., Shields, J., Ducea, M. N., and Saleeby, J. (2020). Fate of the lower lithosphere during shallow-angle subduction: The Laramide example. *GSA Today*, v. 30(1), p. 4-10.

[28]Chapman, A. D., Riggs, N., Ducea, M. N., Saleeby, J. B., Rautela, O., and Shields, J., (2019). Tectonic development of the Colorado Plateau Transition Zone, central Arizona: Insights from lower lithosphere xenoliths and volcanic host rocks. Geologic Excursions in Southwestern North America: *Geological Society of America Field Guide*, v. 55, p. 209-235.

[29]Esperança, S., Carlson, R. W., and Shirey, S. B., (1988). Lower crustal evolution under central Arizona: Sr, Nd and Pb isotopic and geochemical evidence from the mafic xenoliths of Camp Creek. *Earth and Planetary Science Letters*, v. *90*(1), p. 26-40.

[30]Esperança, S., Carlson, R.W., Shirey, S.B., Smith, D., (1997). Dating crust-mantle separation: Re-Os isotopic study of mafic xenoliths from central Arizona. *Geology,* v. 25 (7), p. 651–654. Doi: https://doi.org/10.1130/0091-7613(1997)025<0651:DCMSRO>2.3.CO;2

[31]Loader, M. A., Wilkinson, J. J., and Armstrong, R. N. (2017). The effect of titanite crystallisation on Eu and Ce anomalies in zircon and its implications for the assessment of porphyry Cu deposit fertility. *Earth and Planetary Science Letters*, v. 472, p. 107-119.

[32]Bright, R. M., Amato, J. M., Denyszyn, S. W., and Ernst, R. E., (2014). U-Pb geochronology of 1.1 Ga diabase in the southwestern United States: Testing models for the origin of a post-Grenville large igneous province. *Lithosphere*, v. 6(3), p. 135-156.

[33]Karlstrom, K. E., and Humphreys, E. D., (1998). Persistent influence of Proterozoic accretionary boundaries in the tectonic evolution of southwestern North America: Interaction of cratonic grain and mantle modification events. *Rocky Mountain Geology*, v. 33(2), p. 161-179.

[34]Jacobson, C. E., Hourigan, J. K., Haxel, G. B., and Grove, M., (2017). Extreme latest Cretaceous–Paleogene low-angle subduction: Zircon ages from Orocopia Schist at Cemetery Ridge, southwestern Arizona, USA. *Geology*, v. 45(10), p. 951-954.

[35]Seymour, N. M., Strickland, E. D., Singleton, J. S., Stockli, D. F., and Wong, M. S., (2018). Laramide subduction and metamorphism of the Orocopia Schist, northern Plomosa Mountains, west-central Arizona: Insights from zircon U-Pb geochronology. *Geology*, v. 46(10), p. 847-850.

[36]Haxel, G.B., Epstein, G.S., Jacobson, C.E., Wittke, J.H., Standlee, K.G., and Mulligan, S.R., (2022). Mantle peridotite and associated metasomatic rocks in the Orocopia Schist subduction channel (latest Cretaceous) at Cemetery Ridge, southwest Arizona: Geologic map, petrology, and structural setting: *Arizona Geological Survey Contributed Report* CR-22-A, 85 p., map scale 1:2000.

[37]Hernández-Uribe, D., and Palin, R.M., (2019). Catastrophic shear-removal of subcontinental lithospheric mantle beneath the Colorado Plateau by the subducted Farallon slab. *Scientific Reports*, v. 9, p. 8153 (2019). https://doi.org/10.1038/s41598-019-44628-y

[38]Spencer, J. E., (1996). Uplift of the Colorado Plateau due to lithosphere attenuation during Laramide low-angle subduction, *Journal of Geophysical Research*, v. 101(B6), p. 13595– 13609, doi:10.1029/96JB00818.

[39]Sillitoe, R. H., Creaser, R. A., Kern, R. R., and Lenters, M. H., (2014). Squaw peak, Arizona: Paleoproterozoic precursor to the Laramide porphyry copper province. *Economic Geology*, v. 109 (5), p. 1171–1177. Doi: https://doi.org/10.2113/econgeo.109.5.1171

[40]Reynolds, S. J., Richard, S. M., Haxel, G. B., Tosdal, R. M., and Laubach, S.E., (1988). Geologic setting of Mesozoic and Cenozoic metamorphism in Arizona. W.G Ernst (Ed.), *Metamorphism and Crustal Evolution of the Western United States—The Rubey Volume*, Prentice-Hall, Englewood Cliffs, New Jersey (1988), p. 466-501

[41]Boettcher, S. S., Mosher, S., and Tosdal, R. M., (2002). Structural and tectonic evolution of Mesozoic basement-involved fold nappes and thrust faults in the Dome Rock Mountains, Arizona, *Contributions to Crustal Evolution of the Southwestern United States*, Andrew Barth. https://doi.org/10.1130/0-8137-2365-5.73

[42]Bryant, Bruce, and Wooden, J.L., (2008). Geology of the Northern Part of the Harcuvar Complex, West-Central Arizona: U.S. *Geological Survey Professional Paper* v. 1752, p. 52.

[43]Laubach, S. E., Reynolds, S. J., Spencer, J. E., and Marshak, S., (1989). Progressive deformation and superposed fabrics related to Cretaceous crustal underthrusting in western Arizona, USA. *Journal of Structural Geology*, v. 11, p. 735-749, https://doi.org/10.1016/0191-8141(89)90008-4.

[44]Richard, S. M., Fryxell, J.E., and Sutter, J.F., (1990). Tertiary structure and thermal history of the Harquahala and Buckskin Mountains, west central Arizona: Implications for denudation by a major detachment fault system: *Journal of Geophysical Research*, v. 95(B12), p. 19,973-19,987.

[45]Knapp, J. H., and Heizler, M. T., (1990). Thermal history of crystalline nappes of the Maria fold and thrust belt, west central Arizona. *Journal of Geophysical Research: Solid Earth*, v. 95(B12), p. 20049-20073.

[46]Reynolds, S.J., Spencer, J.E., Laubach, S.E., Cunningham, Dickson, and Richard, S.M., (1991) Geologic map and sections of the Granite Wash Mountains, west-central Arizona [Harcuvar 7.5 min]: *Arizona Geological Survey Map* M-30, 1 sheet, scale 1:24,000.

[47]Wong, M. S., Singleton, J. S., Seymour, N. M., Gans, P. B., and Wrobel, A. J., (2023). Late Cretaceous-early Paleogene extensional ancestry of the Harcuvar and Buckskin-Rawhide metamorphic core complexes, western Arizona. *Tectonics*, v. 42, e2022TC007656. https://doi.org/10.1029/2022TC007656

[48]Lamont, T. N., Searle, M. P., Waters, D. J., Roberts, N. M., Palin, R. M., Smye, A., Gopon, P., Dyck, B., Weller, O., and St-Onge, M. R., (2020). Compressional origin of the Naxos metamorphic core complex, Greece: structure, petrography, and thermobarometry. *Geological Society of America Bulletin*, v. 132(1-2), p. 149-197.

[49]Howard, K. A., and John, B. E., (1987). Crustal extension along a rooted system of imbricate low-angle faults: Colorado River extensional corridor, California and Arizona, in Continental Extensional Tectonics, edited by M. P. Coward, J. F. Dewey, and P. L. Hancock, *Geological Society of London, Special Publications*., v. 28, p. 299–311.

[50]Spencer, J. E., and Reynolds S. J., (1989a). Middle Tertiary tectonics of Arizona and the Southwest, in Geologic Evolution of Arizona, *Arizona Geological Society Digest*, v. 17, edited by J. P. Jenney and S. J. Reynolds, p. 539–574, Arizona Geological Survey, Tucson.

[51]Kohn, M. J., and Spear, F., (2000). Retrograde net transfer reaction insurance for pressure-temperature estimates. *Geology*, v. 28(12), p. 1127-1130.

[52]Dyck, B., Waters, D. J., St-Onge, M. R., and Searle, M. P., (2020). Muscovite dehydration melting: Reaction mechanisms, microstructures, and implications for anatexis. *Journal of Metamorphic Geology*, v. 38(1), p. 29-52.

[53]Weinberg, R. F., and Hasalová, P., (2015). Water-fluxed melting of the continental crust: A review. *Lithos*, v. 212, p. 158-188.

[54]Shafiqullah, M., Damon, P.E., Lynch, D.J., Reynolds, S.J., Rehrig, W.A., and Raymond, R.H., (1980). K-Ar Geochronology and Geologic History Of Southwestern Arizona and Adjacent Areas. *Arizona Geological Society Digest*, v. 12, p. 201-260.

[55]Oriolo, S., Wemmer, K., Oyhantçabal, P., Fossen, H., Schulz, B., and Siegesmund, S., (2018). Geochronology of shear zones–A review. *Earth-Science Reviews*, v. 185, p. 665-683.

[56]Prior, M. G., Stockli, D. F., and Singleton, J. S., (2016). Miocene slip history of the Eagle Eye detachment fault, Harquahala Mountains metamorphic core complex, west-central Arizona, *Tectonics,* v. 35, p. 1913–1934, doi:10.1002/2016TC004241.

[57]Richard, S.M., McWilliams, M.O., and Gans, P.B., (1998). $^{40}Ar/^{39}Ar$ dates from the Harquahala and Little Harquahala Mountains, west-central Arizona. Part I: *Arizona Geological Survey Open-File Report* 98-25, p. 25.

[58]Singleton, J. S., Stockli, D. F., Gans, P. B., and Prior, M. G., (2014). Timing, rate, and magnitude of slip on the Buckskin-Rawhide detachment fault, west central Arizona, *Tectonics*, v. 33, p. 1596–1615, doi:10.1002/2013TC003517.

[59]Boettcher, S.S., Mosher, S., and Tosdal, R.M., (2002). Structural and tectonic evolution of Mesozoic basement-involved fold nappes and thrust faults in the Dome Rock Mountains, Arizona, *Contributions to Crustal Evolution of the Southwestern United States*, Andrew Barth

[60]Affinati, S. C., Hoisch, T. D., Wells, M. L., and Wright, S., (2022). Retroarc Jurassic burial and exhumation of Barrovian metamorphic rocks dated by monazite petrochronology, Funeral Mountains, California, *Tectonic Evolution of the Sevier-Laramide Hinterland, Thrust Belt, and Foreland, and Postorogenic Slab Rollback*

(180–20 Ma), John P. Craddock, David H. Malone, Brady Z. Foreman, Alexandros Konstantinou

[61]Isachen, C., Gehrels, G., Riggs, N., Spencer, J., Ferguson, C., Skotnicki, S., and Richard, S, (1999). U-Pb geochronological data from zircons from eleven granitic rocks in central and Western Arizona; *Arizona Geological Survey Open File Report* 99-2

[62]DeWitt, E. and Reynolds, S. J., (1990). Late Cretaceous plutonism and cooling in the Maria fold and thrust belt, west central *Arizona Geological Society America Abstract*. Programs, v. 22, p. 18.

[63]Knapp, J.H., (2018). Mesozoic Thrusting and Tertiary Detachment Faulting in the Moon Mountains, west-central Arizona. *Arizona Geological Survey Contributed Report CR-18-I*, 56 p.

[64]Shehata, M.A., and Mizunaga, H. (2022). Moho depth and tectonic implications of the western United States: insights from gravity data interpretation. *Geoscience Letters,* v. 9, p. 23. https://doi.org/10.1186/s40562-022-00233-y.

[65]Chapman, J. B., Greig,R., and Haxel, G.B., (2020). Geochemical evidence for an orogenic plateau in the southern US and northern Mexican Cordillera during the Laramide orogeny. *Geology,* v. 48, p. 164-168.

[66]Barra, F., Ruiz, J., Mathur, R., and Titley, S., (2003). A Re–Os study of sulfide minerals from the Bagdad porphyry Cu–Mo deposit, northern Arizona, USA. *Miner Deposita* 38, v. 585–596 (2003). https://doi.org/10.1007/s00126-002-0341-0.

[67]English, J. M., Johnston, S. T., & Wang, K. (2003). Thermal modelling of the Laramide orogeny: testing the flat-slab subduction hypothesis. *Earth and Planetary Science Letters*, v. 214(3-4), p. 619-632.

[68]England, P. C., and Thompson, A. B., (1984). Pressure—temperature—time paths of regional metamorphism I. Heat transfer during the evolution of regions of thickened continental crust. *Journal of Petrology*, v. 25(4), p. 894-928.

[69]Smith, D., Arculus, R. J., Manchester, J. E., and Tyner, G. N. (1994). Garnet-pyroxene-amphibole xenoliths from Chino Valley, Arizona, and implications for continental lithosphere below the Moho, *Journal of Geophysical Research*, v. 99 (B1), p. 683–696, doi:10.1029/93JB02994.

[70]Beard, J. E., and Lofgren, G. E., (1991). Dehydration Melting and Water-Saturated Melting of Basaltic and Andesitic Greenstones and Amphibolites at 1, 3, and 6. 9 kb, *Journal of Petrology*, v. 32, p. 365–401, https://doi.org/10.1093/petrology/32.2.365

[71]Zhang, J., Chang, J., Wang, R. and Audétat, A., (2022). Can Post-Subduction Porphyry Cu Magmas Form by Partial Melting of Typical Lower Crustal Amphibole-Rich Cumulates? Petrographic and Experimental Constraints from Samples of the

Kohistan and Gangdese Arc Roots. *Journal of Petrology*, v. 63(11), egac101, https://doi.org/10.1093/petrology/egac101.

[72]Wang, X., Sun, M., Weinberg, R.F., Cai, K., Zhao, G., Xia, X., Li, P. and Liu, X., (2022). Adakite generation as a result of fluid-fluxed melting at normal lower crustal pressures. *Earth and Planetary Science Letters*, v. 594, p.117744.

[73]Yakymchuk, C., Holder, R. M., Kendrick, J., and Moyen, J.F., (2023). Europium anomalies in zircon: A signal of crustal depth? Earth and Planetary Science Letters, v. 622, 118405, https://doi.org/10.1016/j.epsl.2023.118405.

[74]Whitney, D. L., and Evans, B. W. (2010). Abbreviations for names of rock-forming minerals. *The American mineralogist*, v. 95(1), p. 185-187.

[75]Howie, R. A., Zussman, J., and Deer, W. (1992). An introduction to the rock-forming minerals (p. 696). London, UK: Longman.

[76]Holland, T.J., (2009). AX: A program to calculate activities of mineral end-members from chemical analyses: http://www.esc.cam.ac.uk/research/research-groups/holland/ax

[77]Henry, D.J., Guidotti, C.V., and Thomson, J.A., (2005). The Ti-saturation surface for low-to-medium pressure metapelitic biotite: Implications for geothermometry and Ti-substitution mechanisms: *The American Mineralogist*, v. 90, p. 316–328, https://doi.org/10.2138/am.2005.1498.

[78]Spear, F.S., (1993). Metamorphic Phase Equilibria and Pressure-Temperature-Time Paths, *Mineralogical Society of America Monograph,* v. 1, p. 799.

[79]Bhattacharya, L., Mohanty, L., Maji, A., Sen, S.K., and Raith, M., (1992). Non-ideal mixing in the phlogopite-annite binary: Constraints from experimental data on Mg-Fe partitioning and a reformulation of the biotite-garnet geothermometer*: Contributions to Mineralogy and Petrology*, v. 111, p. 87–93, https://doi.org/10.1007/BF00296580.

[80]Powell, R., and Holland, T. J., (2008). On thermobarometry, *Journal of Metamorphic Geology*, v. 26, p. 155–179, https://doi.org/10.1111/j.1525-1314.2007.00756.x.

[81]de Capitani C. and Petrakakis K. (2010). The computation of equilibrium assemblage diagrams with Theriak/Domino software. American Mineralogist, v. 95, p. 1006–1016.

[82]Holland, T. J. B., and Powell, R. (2011). An improved and extended internally consistent thermodynamic dataset for phases of petrological interest, involving a new equation of state for solids. *Journal of Metamorphic Geology*. v. 29, p. 333–383.

[83]Green, E. C. R., White, R. W., Diener, J. F. A., Powell, R., Holland, T. J. B., and Palin, R. M. (2016). Activity–composition relations for the calculation of partial melting equilibria in metabasic rocks. *Journal of metamorphic Geology*, v. 34(9), p. 845-869.

[84]White, R. W., Powell, R. O. G. E. R., Holland, T. J. B., Johnson, T. E., and Green, E. C. R. (2014). New mineral activity–composition relations for thermodynamic

calculations in metapelitic systems. *Journal of Metamorphic Geology*, v. 32(3), p. 261-286.

[85]Holland, T.J.B., Green, E.C.R. and Powell, R. (2022) A thermodynamic model for feldspars in $KAlSi_3O_8$−$NaAlSi_3O_8$−$CaAl_2Si_2O_8$ for mineral equilibrium calculations. *Journal of Metamorphic Geology*, v. 40 (4), p. 587– 600. https://doi.org/10.1111/jmg.12639

[86]Carson, C. J., Powell, R. and Clarke, G. (1999) Calculated mineral equilibria for eclogites in CaO–Na2O–FeO–MgO–Al2O3–SiO2–H2O: Application to the Pouebo Terrane, Pam Peninsula, New Caledonia. *Journal of Metamorphic Geology*. v. 17, p. 9–24.

[87]Palin, R. M., Weller, O. M., Waters, D. J., and Dyck, B. (2016). Quantifying geological uncertainty in metamorphic phase equilibria modelling; a Monte Carlo assessment and implications for tectonic interpretations. *Geoscience Frontiers*, v. 7(4), p. 591-607.

[88]Villa, I.M., Holden, N.E., Possolo, A., Ickert, R.B., Hibbert, D.B. and Renne, P.R., (2020). IUPAC-IUGS recommendation on the half-lives of ^{147}Sm and ^{146}Sm. *Geochimica et cosmochimica acta*, v. 285, p. 70-77.

[89]Bouvier, A., Vervoort, J. D., and Patchett, P. J. (2008). The Lu–Hf and Sm–Nd isotopic composition of CHUR: constraints from unequilibrated chondrites and implications for the bulk composition of terrestrial planets. *Earth and Planetary Science Letters*, v. 273(1-2), p. 48-57.

[90]Taylor, S R, and McLennan, S M. (1985). The continental crust: Its composition and evolution. United States.

[91]Pearson, D. G., Shirey, S. B., Carlson, R.W., Boyd, F.R., Pokhilenko, N.P., and Shimizu, N., (1995). Re-Os, Sm-Nd, and Rb-Sr isotope evidence for thick Archaean lithospheric mantle beneath the Siberian craton modified by multistage metasomatism, *Geochimica et Cosmochimica Acta*, v. 59, p. 959-977, https://doi.org/10.1016/0016-7037(95)00014-3.

[92]Bevan, D., Coath, C.D., Lewis, J., Schwieters, J., Lloyd, N., Craig, G., Wehrs, H. and Elliott, T., (2021). In situ Rb–Sr dating by collision cell, multicollection inductively-coupled plasma mass-spectrometry with pre-cell mass-filter, (CC-MC-ICPMS/MS). *Journal of analytical atomic spectrometry*, v. 36(5), p. 917–931.

[93]Craig, G., Managh, A. J., Stremtan, C., Lloyd, N. S. and Horstwood, M. S. A. (2018) Doubling Sensitivity in Multicollector ICPMS Using High-Efficiency, Rapid Response Laser Ablation Technology. *Analytical Chemistry*. V. 90, p. 11564–11571.

[94]Cheng, P., Koyanagi, G. K. and Bohme, D. K. (2008) On the chemical resolution of the $^{87}Rb+$ (s0)/$^{87}Sr+$ (s1) isobaric interference: A kinetic search for an optimum reagent. *Analytica Chimica Acta* v. 627, p. 148–153.

[95]Hogmalm, K. J., Zack, T., Karlsson, A. K.-O., Sjöqvist, A. S. L. and Garbe-Schönberg, D., (2017). In situ Rb–Sr and K–Ca dating by LA-ICP-MS/MS: an evaluation of N 2 O and SF 6 as reaction gases. *J. Anal. At. Spectrom*. V. 32, p. 305–313.

[96]Koornneef, J. M., Bouman, C., Schwieters, J. B. and Davies, G. R., (2014). Measurement of small ion beams by thermal ionisation mass spectrometry using new 1013Ohm resistors. Analytica Chimica Acta v. 819, p. 49–55.

[97]Klaver, M., Smeets, R. J., Koornneef, J. M., Davies, G. R. and Vroon, P. Z., (2016). Pb isotope analysis of ng size samples by TIMS equipped with a 10 13 Ω resistor using a 207 Pb– 204 Pb double spike. J. Anal. At. Spectrom. V. 31, p. 171–178 (2016).

[98]Kimura, J.-I., Chang, Q., Kanazawa, N., Sasaki, S. and Vaglarov, B. S, (2016). High-precision in situ analysis of Pb isotopes in glasses using 10 13 Ω resistor high gain amplifiers with ultraviolet femtosecond laser ablation multiple Faraday collector inductively coupled plasma mass spectrometry. J. Anal. At. Spectrom. v. 31, p. 790–800.

[99]Vermeesch, P., (2018). IsoplotR: A free and open toolbox for geochronology. *Geoscience Frontiers*, v. 9, 1479–1493 (2018).

[100]Regis, D., Warren, C.J., Mottram, C.M. and Roberts, N.M., (2016). Using monazite and zircon petrochronology to constrain the P–T–t evolution of the middle crust in the Bhutan Himalaya. *Journal of Metamorphic Geology*, v. *34*(6), p. 617-639.

[101]Paton, C., Hellstrom, J., Paul, B., Woodhead, J. and Hergt, J., (2011). Iolite: Freeware for the visualisation and processing of mass spectrometric data. *Journal of Analytical Atomic Spectrometry*, v. *26*(12), p. 2508-2518.

[102]Aleinikoff, J.N., Schenck, W.S., Plank, M.O., Srogi, L., Fanning, C.M., Kamo, S.L. and Bosbyshell, H., (2006). Deciphering igneous and metamorphic events in high-grade rocks of the Wilmington Complex, Delaware: Morphology, cathodoluminescence and backscattered electron zoning, and SHRIMP U-Pb geochronology of zircon and monazite. *Geological Society of America Bulletin*, v. 118(1-2), p. 39-64.

[103]Gonçalves, G.O., Lana, C., Scholz, R., Buick, I.S., Gerdes, A., Kamo, S.L., Corfu, F., Marinho, M.M., Chaves, A.O., Valeriano, C. and Nalini Jr, H.A., (2016). An assessment of monazite from the Itambé pegmatite district for use as U–Pb isotope reference material for microanalysis and implications for the origin of the “Moacyr” monazite. *Chemical Geology*, v. 424, p. 30-50.

[104]Wong, M. S., and Gans, P., (2008). Geologic, structural, and thermochronologic constraints on the tectonic evolution of the Sierra Mazatán core complex, Sonora, Mexico, Tectonics, v. 27, TC4013.

[105]Hodges, K. V., and Walker, J. D., (1992). Extension in the Cretaceous Sevier orogen, North American Cordillera, *Geological Society of America Bulletin*, v. 104, p. 560–569.

[106]Dave, R., and Li, A., (2016). Destruction of the Wyoming craton: Seismic evidence and geodynamic processes, *Geology*, v. 44, p. 883–886.

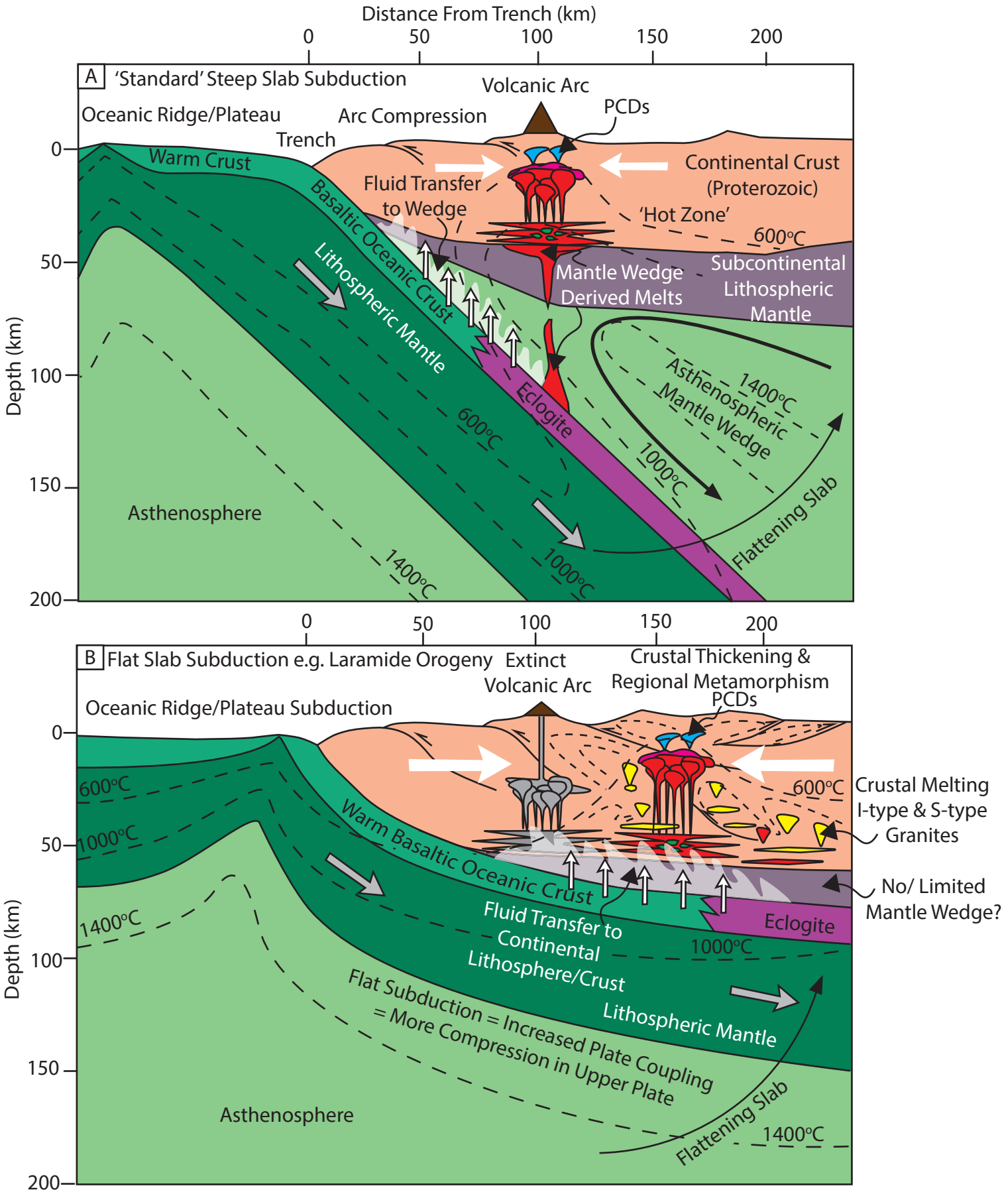
Distance From Trench (km)
0
50
100
150
200
A 'Standard' Steep Slab Subduction
Volcanic Arc
PCDs
Oceanic Ridge/Plateau
Arc Compression
Trench
Warm Crust
Fluid Transfer to Wedge
Continental Crust (Proterozoic)
'Hot Zone'
600°C
Basaltic Oceanic Crust
Lithospheric Mantle
Mantle Wedge Derived Melts
Subcontinental Lithospheric Mantle
Asthenospheric Mantle Wedge
1400°C
1000°C
Eclogite
Flattening Slab
Asthenosphere
Depth (km)
0
50
100
150
200
B Flat Slab Subduction e.g. Laramide Orogeny
Extinct Volcanic Arc
Crustal Thickening & Regional Metamorphism
PCDs
Oceanic Ridge/Plateau Subduction
600°C
1000°C
1400°C
Warm Basaltic Oceanic Crust
Crustal Melting I-type & S-type Granites
No/ Limited Mantle Wedge?
Fluid Transfer to Continental Lithosphere/Crust
Eclogite
Lithospheric Mantle
Flat Subduction = Increased Plate Coupling = More Compression in Upper Plate
Asthenosphere
Flattening Slab

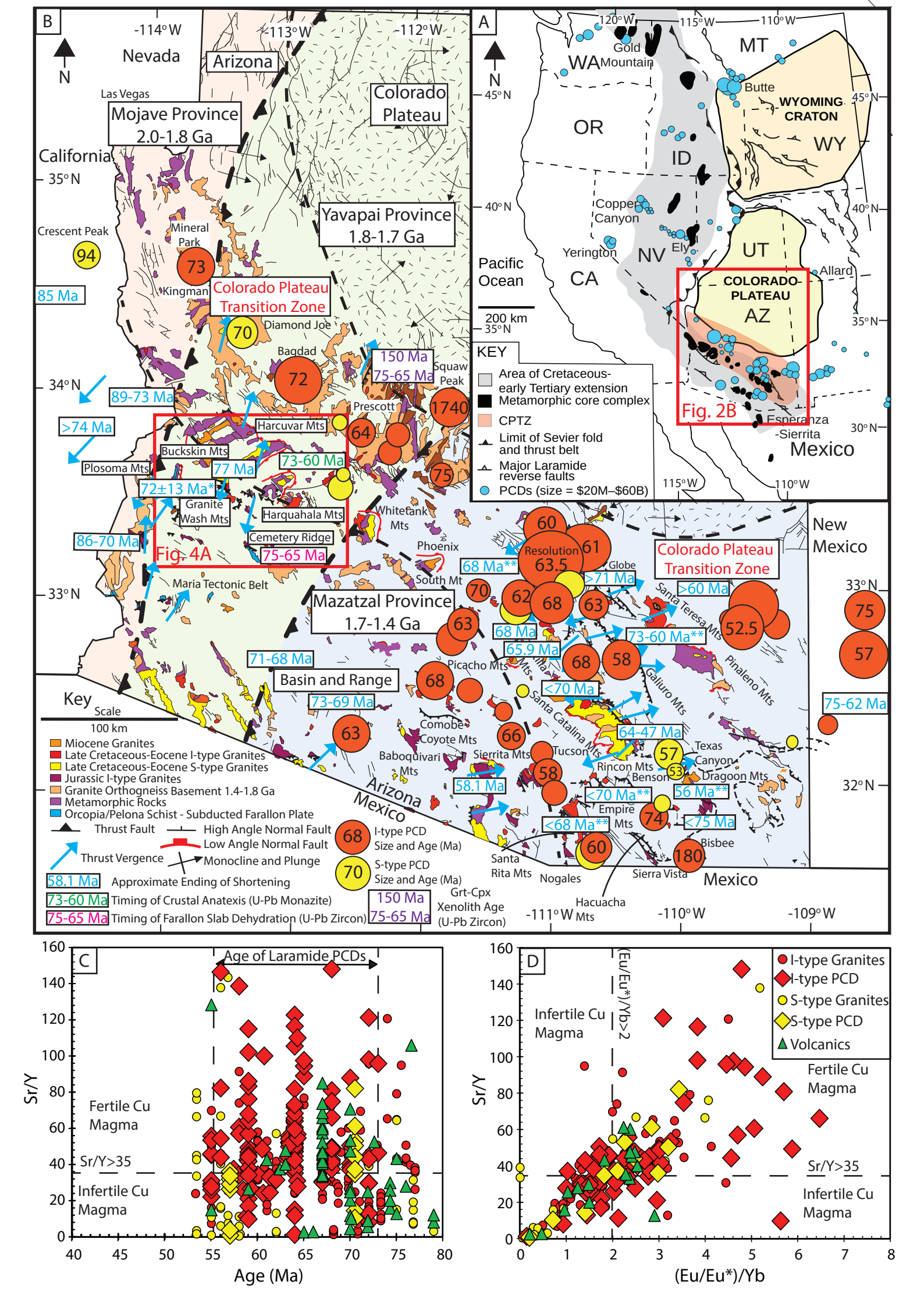
B
A
Nevada
Arizona
California
New Mexico
Mexico
Las Vegas
Mojave Province
2.0-1.8 Ga
Colorado Plateau
Yavapai Province
1.8-1.7 Ga
Mazatzal Province
1.7-1.4 Ga
Basin and Range
Colorado Plateau Transition Zone
Fig. 4A
Fig. 2B
Crescent Peak
Mineral Park
Kingman
Diamond Joe
Baggdad
Squaw Peak
Prescott
Harcuvar Mts
Buckskin Mts
Plosoma Mts
Granite Wash Mts
Harquahala Mts
Cemetery Ridge
Whitetank Mts
Phoenix
South Mt
Maria Tectonic Belt
Resolution
Globe
Picacho Mts
Comobe
Coyote Mts
Baboquivari Mts
Sierrita Mts
Tucson
Rincon Mts
Santa Catalina Mts
Santa Teresa Mts
Galiuro Mts
Pinaleno Mts
Texas Canyon
Dragoon Mts
Benson
Empire Mts
Bisbee
Sierra Vista
Santa Rita Mts
Nogales
Hacuacha Mts
Esperanza-Sierrita
WA
OR
CA
ID
NV
MT
WY
UT
AZ
Gold Mountain
Butte
WYOMING CRATON
Copper Canyon
Yerington
Ely
Allard
COLORADO-PLATEAU
Pacific Ocean
200 km
KEY
Area of Cretaceous-early Tertiary extension
Metamorphic core complex
CPTZ
Limit of Sevier fold and thrust belt
Major Laramide reverse faults
PCDs (size = $20M–$60B)
85 Ma
89-73 Ma
>74 Ma
77 Ma
72±13 Ma*
86-70 Ma
73-60 Ma
75-65 Ma
150 Ma
68 Ma**
>71 Ma
>60 Ma
73-60 Ma**
65.9 Ma
71-68 Ma
73-69 Ma
<70 Ma
64-47 Ma
58.1 Ma
<70 Ma**
56 Ma**
<68 Ma**
<75 Ma
75-62 Ma
Key
Scale
100 km
Miocene Granites
Late Cretaceous-Eocene I-type Granites
Late Cretaceous-Eocene S-type Granites
Jurassic I-type Granites
Granite Orthogneiss Basement 1.4-1.8 Ga
Metamorphic Rocks
Orcopia/Pelona Schist - Subducted Farallon Plate
Thrust Fault
High Angle Normal Fault
Low Angle Normal Fault
Thrust Vergence
Monocline and Plunge
Approximate Ending of Shortening
Timing of Crustal Anatexis (U-Pb Monazite)
Timing of Farallon Slab Dehydration (U-Pb Zircon)
I-type PCD Size and Age (Ma)
S-type PCD Size and Age (Ma)
Grt-Cpx Xenolith Age (U-Pb Zircon)

C
Age of Laramide PCDs
Fertile Cu Magma
Sr/Y>35
Infertile Cu Magma
Sr/Y
Age (Ma)

D
I-type Granites
I-type PCD
S-type Granites
S-type PCD
Volcanics
Infertile Cu Magma
(Eu/Eu*)/Yb>2
Fertile Cu Magma
Sr/Y>35
Infertile Cu Magma
Sr/Y
(Eu/Eu*)/Yb

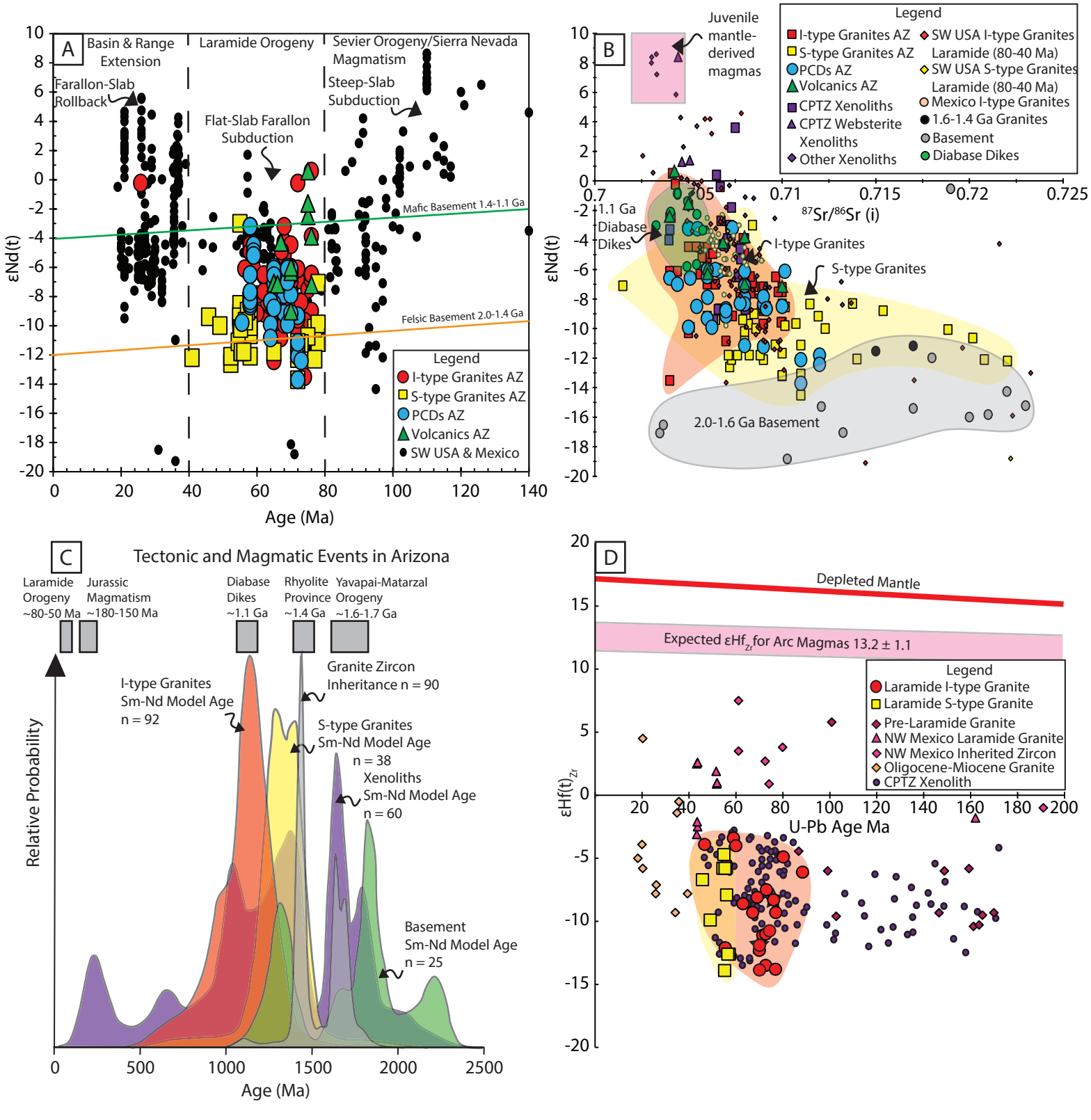
A
Basin & Range Extension
Laramide Orogeny
Sevier Orogeny/Sierra Nevada Magmatism
Farallon-Slab Rollback
Flat-Slab Farallon Subduction
Steep-Slab Subduction
Mafic Basement 1.4-1.1 Ga
Felsic Basement 2.0-1.4 Ga
Legend
I-type Granites AZ
S-type Granites AZ
PCDs AZ
Volcanics AZ
SW USA & Mexico
εNd(t)
Age (Ma)
B
Juvenile mantle-derived magmas
Legend
I-type Granites AZ
S-type Granites AZ
PCDs AZ
Volcanics AZ
CPTZ Xenoliths
CPTZ Websterite Xenoliths
Other Xenoliths
SW USA I-type Granites Laramide (80-40 Ma)
SW USA S-type Granites Laramide (80-40 Ma)
Mexico I-type Granites
1.6-1.4 Ga Granites
Basement
Diabase Dikes
1.1 Ga Diabase Dikes
I-type Granites
S-type Granites
2.0-1.6 Ga Basement
εNd(t)
87Sr/86Sr (i)
C
Tectonic and Magmatic Events in Arizona
Laramide Orogeny ~80-50 Ma
Jurassic Magmatism ~180-150 Ma
Diabase Dikes ~1.1 Ga
Rhyolite Province ~1.4 Ga
Yavapai-Matarzal Orogeny ~1.6-1.7 Ga
I-type Granites Sm-Nd Model Age n = 92
Granite Zircon Inheritance n = 90
S-type Granites Sm-Nd Model Age n = 38
Xenoliths Sm-Nd Model Age n = 60
Basement Sm-Nd Model Age n = 25
Relative Probability
Age (Ma)
D
Depleted Mantle
Expected εHfZr for Arc Magmas 13.2 ± 1.1
Legend
Laramide I-type Granite
Laramide S-type Granite
Pre-Laramide Granite
NW Mexico Laramide Granite
NW Mexico Inherited Zircon
Oligocene-Miocene Granite
CPTZ Xenolith
εHf(t)Zr
U-Pb Age Ma

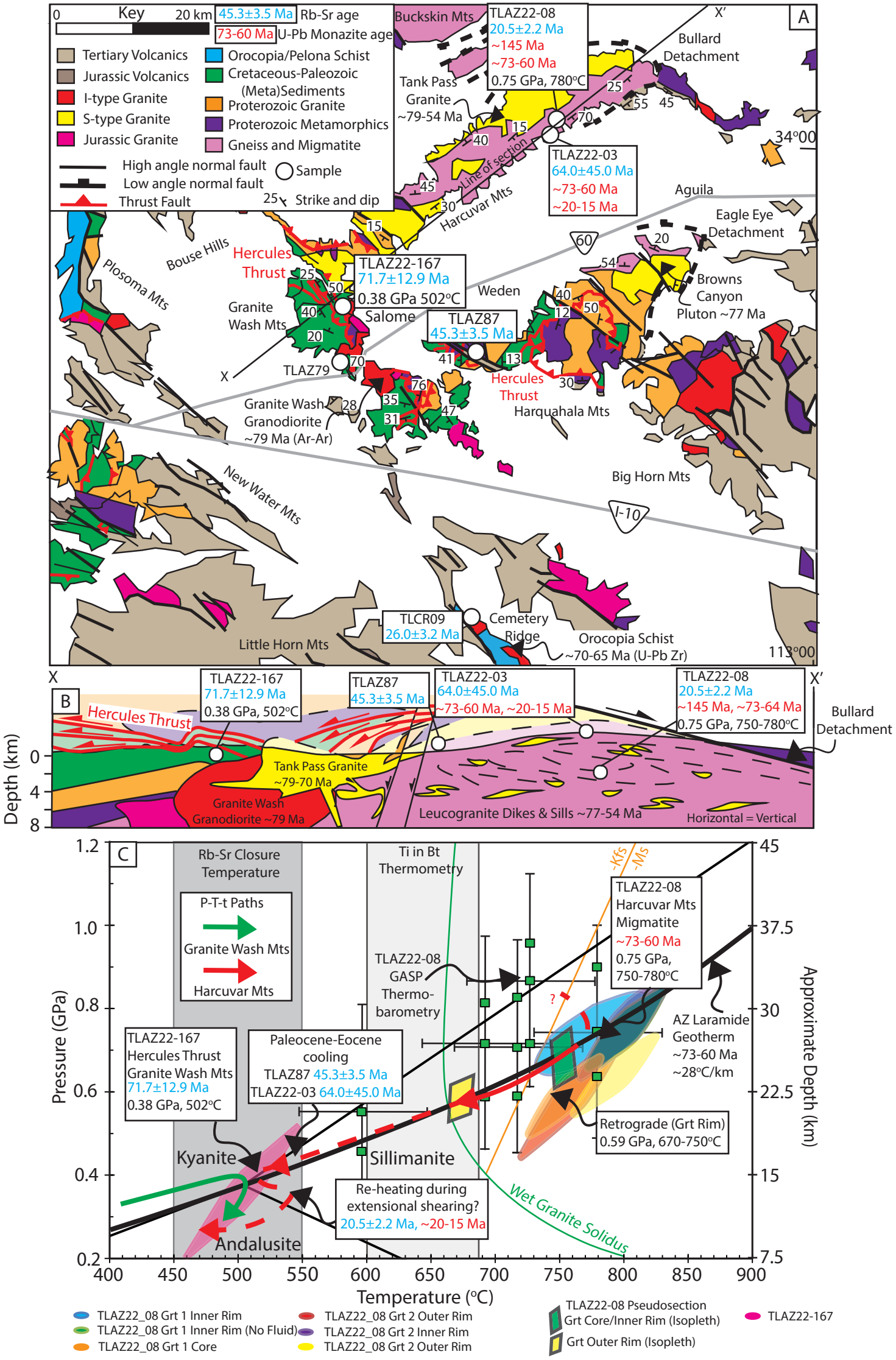
A
Key
0
20 km
45.3±3.5 Ma Rb-Sr age
73-60 Ma U-Pb Monazite age
Tertiary Volcanics
Jurassic Volcanics
I-type Granite
S-type Granite
Jurassic Granite
Orocopia/Pelona Schist
Cretaceous-Paleozoic (Meta)Sediments
Proterozoic Granite
Proterozoic Metamorphics
Gneiss and Migmatite
High angle normal fault
Low angle normal fault
Thrust Fault
Sample
Strike and dip
Buckskin Mts
TLAZ22-08
20.5±2.2 Ma
~145 Ma
~73-60 Ma
0.75 GPa, 780°C
X'
Bullard Detachment
Tank Pass Granite ~79-54 Ma
TLAZ22-03
64.0±45.0 Ma
~73-60 Ma
~20-15 Ma
Line of section
Harcuvar Mts
Aguila
Eagle Eye Detachment
Bouse Hills
Plosoma Mts
Hercules Thrust
TLAZ22-167
71.7±12.9 Ma
0.38 GPa 502°C
Salome
Granite Wash Mts
Weden
Browns Canyon Pluton ~77 Ma
TLAZ87
45.3±3.5 Ma
TLAZ79
X
Granite Wash Granodiorite ~79 Ma (Ar-Ar)
Hercules Thrust
Harquahala Mts
New Water Mts
Big Horn Mts
I-10
TLCR09
26.0±3.2 Ma
Cemetery Ridge
Orocopia Schist ~70-65 Ma (U-Pb Zr)
Little Horn Mts
34°00
113°00
B
X
X'
TLAZ22-167
71.7±12.9 Ma
0.38 GPa, 502°C
TLAZ87
45.3±3.5 Ma
TLAZ22-03
64.0±45.0 Ma
~73-60 Ma, ~20-15 Ma
TLAZ22-08
20.5±2.2 Ma
~145 Ma, ~73-64 Ma
0.75 GPa, 750-780°C
Bullard Detachment
Hercules Thrust
Tank Pass Granite ~79-70 Ma
Granite Wash Granodiorite ~79 Ma
Leucogranite Dikes & Sills ~77-54 Ma
Horizontal = Vertical
Depth (km)
0
4
8
C
Rb-Sr Closure Temperature
Ti in Bt Thermometry
P-T-t Paths
Granite Wash Mts
Harcuvar Mts
TLAZ22-08 GASP Thermo-barometry
-Kfs
-Ms
TLAZ22-08
Harcuvar Mts
Migmatite
~73-60 Ma
0.75 GPa,
750-780°C
AZ Laramide Geotherm
~73-60 Ma
~28°C/km
TLAZ22-167
Hercules Thrust
Granite Wash Mts
71.7±12.9 Ma
0.38 GPa, 502°C
Paleocene-Eocene cooling
TLAZ87 45.3±3.5 Ma
TLAZ22-03 64.0±45.0 Ma
Retrograde (Grt Rim)
0.59 GPa, 670-750°C
Kyanite
Sillimanite
Andalusite
Re-heating during extensional shearing?
20.5±2.2 Ma, ~20-15 Ma
Wet Granite Solidus
Pressure (GPa)
Approximate Depth (km)
Temperature (°C)
TLAZ22_08 Grt 1 Inner Rim
TLAZ22_08 Grt 1 Inner Rim (No Fluid)
TLAZ22_08 Grt 1 Core
TLAZ22_08 Grt 2 Outer Rim
TLAZ22_08 Grt 2 Inner Rim
TLAZ22_08 Grt 2 Outer Rim
TLAZ22-08 Pseudosection
Grt Core/Inner Rim (Isopleth)
Grt Outer Rim (Isopleth)
TLAZ22-167

Laramide Crustal Section ~75-50 Ma

Geological Features and Exposure

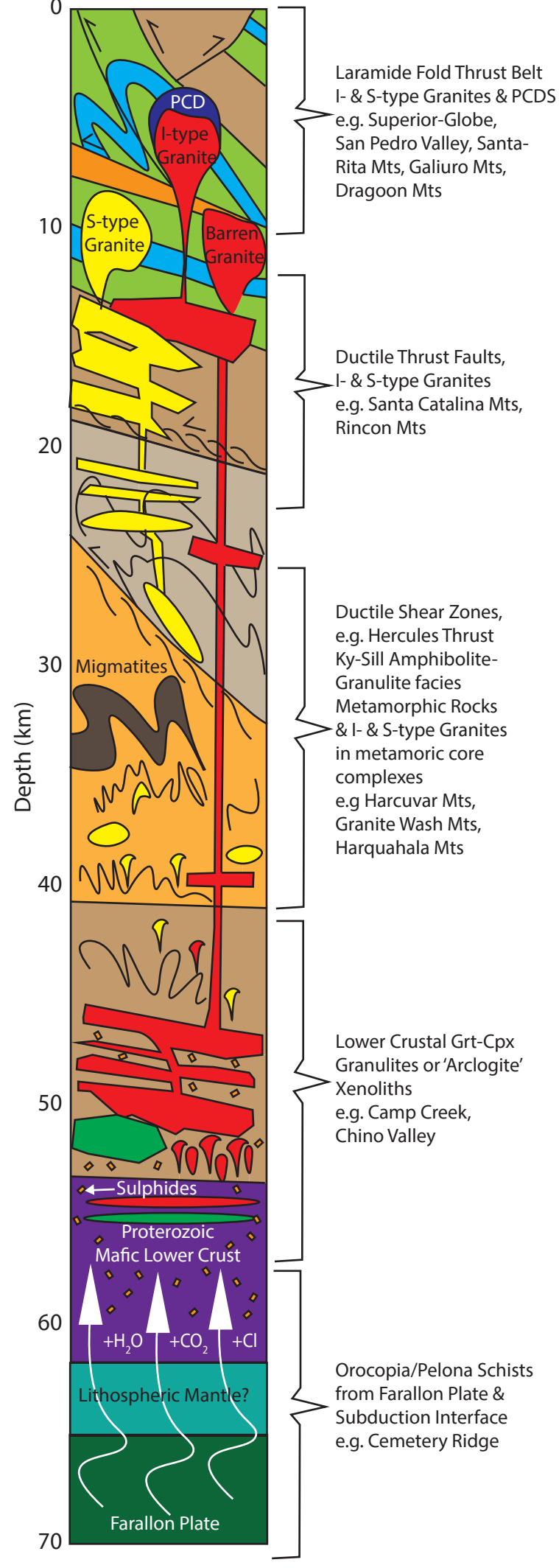

Laramide Fold Thrust Belt
I- & S-type Granites & PCDS
e.g. Superior-Globe, San Pedro Valley, Santa-Rita Mts, Galiuro Mts, Dragoon Mts

Ductile Thrust Faults,
I- & S-type Granites
e.g. Santa Catalina Mts, Rincon Mts

Ductile Shear Zones, e.g. Hercules Thrust
Ky-Sill Amphibolite-Granulite facies Metamorphic Rocks
& I- & S-type Granites in metamoric core complexes
e.g Harcuvar Mts, Granite Wash Mts, Harquahala Mts

Lower Crustal Grt-Cpx Granulites or 'Arclogite' Xenoliths
e.g. Camp Creek, Chino Valley

Orocopia/Pelona Schists from Farallon Plate & Subduction Interface
e.g. Cemetery Ridge

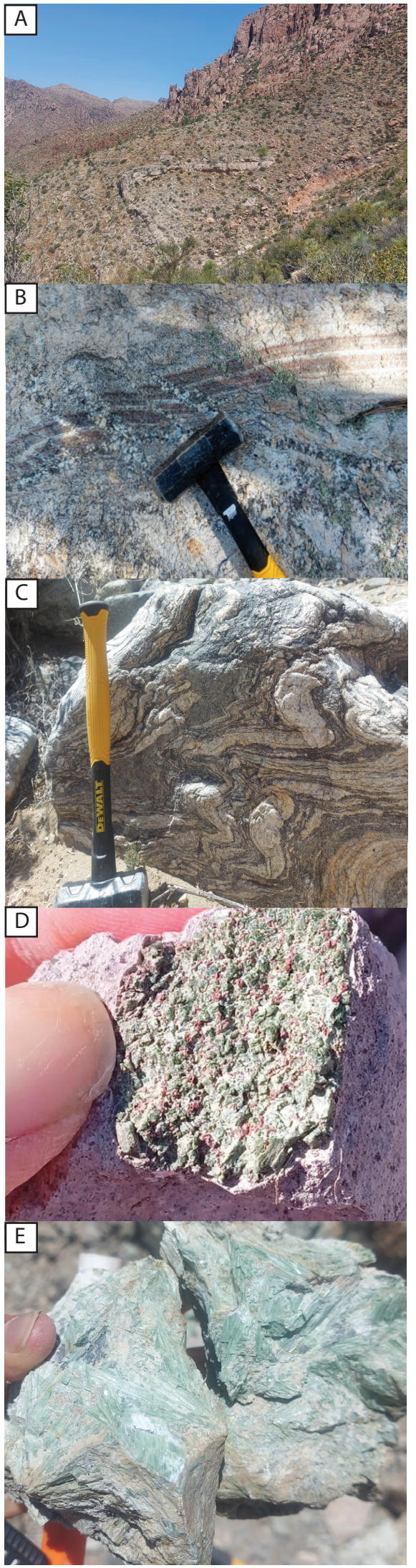

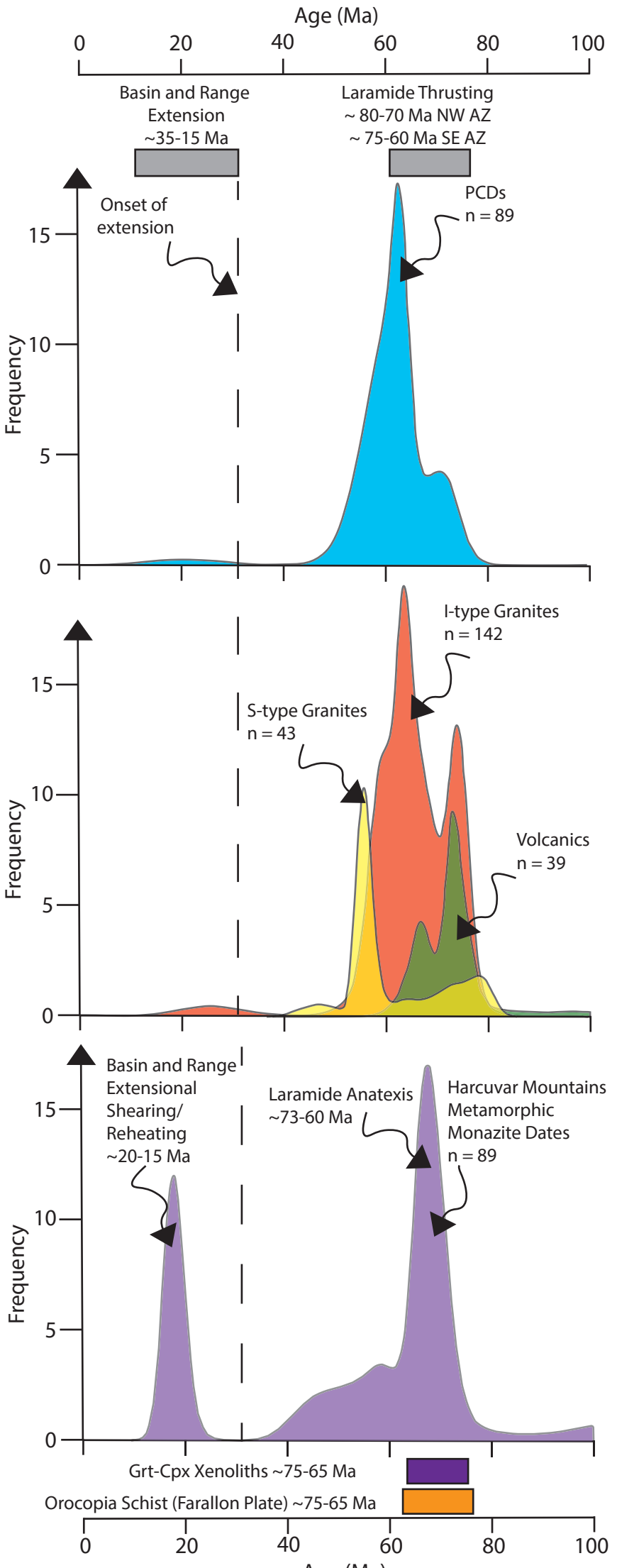

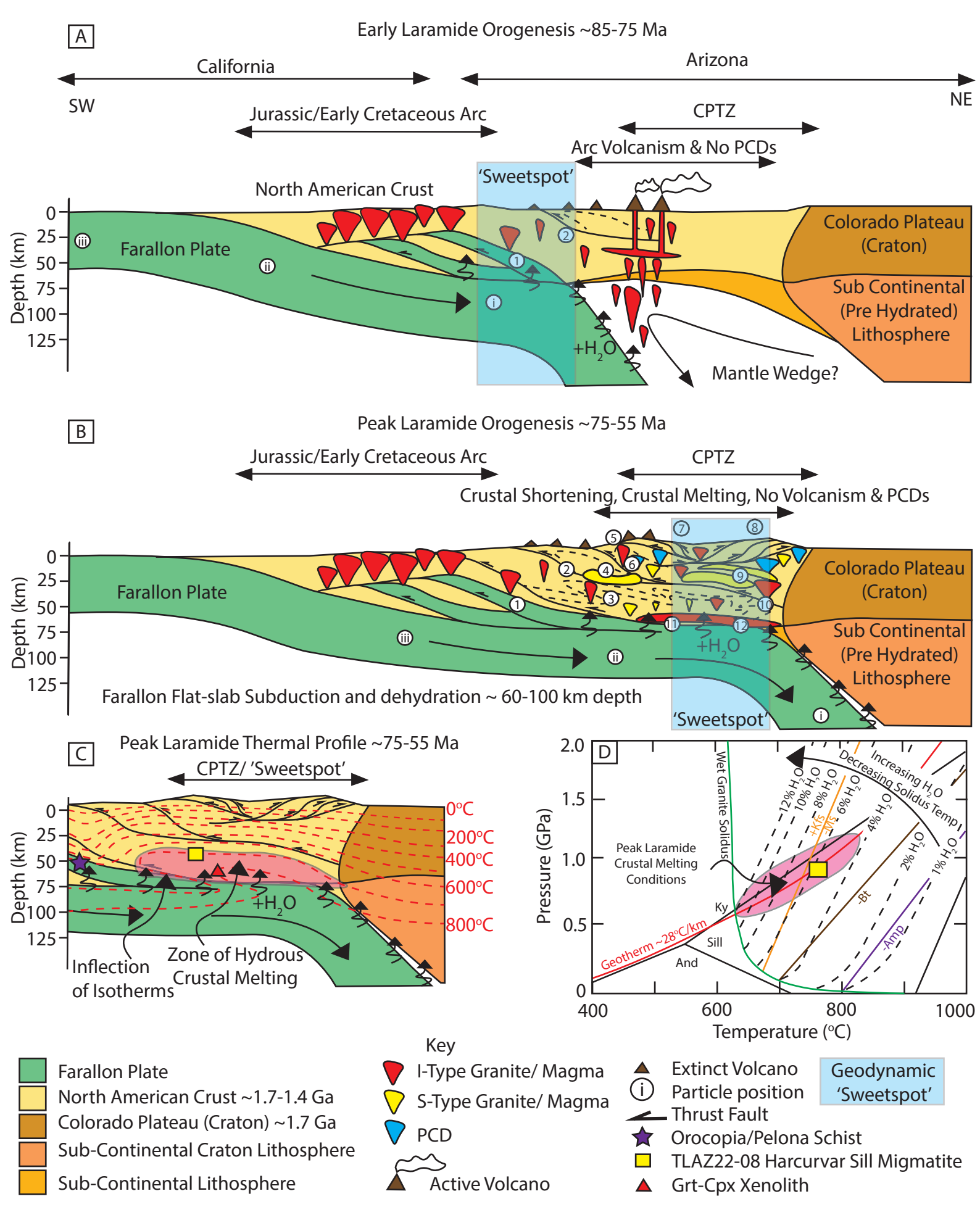
A
Early Laramide Orogenesis ~85-75 Ma
California
Arizona
SW
NE
Jurassic/Early Cretaceous Arc
CPTZ
Arc Volcanism & No PCDs
'Sweetspot'
North American Crust
Depth (km)
0
25
50
75
100
125
Farallon Plate
Colorado Plateau (Craton)
Sub Continental (Pre Hydrated) Lithosphere
+H2O
Mantle Wedge?
B
Peak Laramide Orogenesis ~75-55 Ma
Jurassic/Early Cretaceous Arc
CPTZ
Crustal Shortening, Crustal Melting, No Volcanism & PCDs
Farallon Plate
Colorado Plateau (Craton)
Sub Continental (Pre Hydrated) Lithosphere
+H2O
Farallon Flat-slab Subduction and dehydration ~ 60-100 km depth
'Sweetspot'
C
Peak Laramide Thermal Profile ~75-55 Ma
CPTZ/ 'Sweetspot'
0°C
200°C
400°C
600°C
800°C
+H2O
Inflection of Isotherms
Zone of Hydrous Crustal Melting
D
Pressure (GPa)
Temperature (°C)
Wet Granite Solidus
Peak Laramide Crustal Melting Conditions
Ky
Sill
And
Geotherm ~28°C/km
Increasing H2O
Decreasing Solidus Temp
12% H2O
10% H2O
8% H2O
6% H2O
4% H2O
2% H2O
1% H2O
+Ms
-Ms
-Bt
-Amp
Key
Farallon Plate
North American Crust ~1.7-1.4 Ga
Colorado Plateau (Craton) ~1.7 Ga
Sub-Continental Craton Lithosphere
Sub-Continental Lithosphere
I-Type Granite/ Magma
S-Type Granite/ Magma
PCD
Active Volcano
Extinct Volcano
Particle position
Thrust Fault
Orocopia/Pelona Schist
TLAZ22-08 Harcurvar Sill Migmatite
Grt-Cpx Xenolith
Geodynamic 'Sweetspot'